

Electron and Photon Identification in the D0 Experiment

V.M. Abazov,³¹ B. Abbott,⁶⁷ B.S. Acharya,²⁵ M. Adams,⁴⁶ T. Adams,⁴⁴ J.P. Agnew,⁴¹ G.D. Alexeev,³¹ G. Alkhazov,³⁵ A. Alton^a,⁵⁶ A. Askew,⁴⁴ S. Atkins,⁵⁴ K. Augsten,⁷ C. Avila,⁵ F. Badaud,¹⁰ L. Bagby,⁴⁵ B. Baldin,⁴⁵ D.V. Bandurin,⁷³ S. Banerjee,²⁵ E. Barberis,⁵⁵ P. Baringer,⁵³ J.F. Bartlett,⁴⁵ U. Bassler,¹⁵ V. Bazterra,⁴⁶ A. Bean,⁵³ M. Begalli,² L. Bellantoni,⁴⁵ S.B. Beri,²³ G. Bernardi,¹⁴ R. Bernhard,¹⁹ I. Bertram,³⁹ M. Besançon,¹⁵ R. Beuselinck,⁴⁰ P.C. Bhat,⁴⁵ S. Bhatia,⁵⁸ V. Bhatnagar,²³ G. Blazey,⁴⁷ S. Blessing,⁴⁴ K. Bloom,⁵⁹ A. Boehnlein,⁴⁵ D. Boline,⁶⁴ E.E. Boos,³³ G. Borissov,³⁹ M. Borysova^l,³⁸ A. Brandt,⁷⁰ O. Brandt,²⁰ R. Brock,⁵⁷ A. Bross,⁴⁵ D. Brown,¹⁴ X.B. Bu,⁴⁵ M. Buehler,⁴⁵ V. Buescher,²¹ V. Bunichev,³³ S. Burdin^b,³⁹ C.P. Buszello,³⁷ E. Camacho-Pérez,²⁸ B.C.K. Casey,⁴⁵ H. Castilla-Valdez,²⁸ S. Caughron,⁵⁷ S. Chakrabarti,⁶⁴ K.M. Chan,⁵¹ A. Chandra,⁷² E. Chapon,¹⁵ G. Chen,⁵³ S.W. Cho,²⁷ S. Choi,²⁷ B. Choudhary,²⁴ S. Cihangir,⁴⁵ D. Claes,⁵⁹ J. Clutter,⁵³ M. Cooke^k,⁴⁵ W.E. Cooper,⁴⁵ M. Corcoran,⁷² F. Couderc,¹⁵ M.-C. Cousinou,¹² D. Cutts,⁶⁹ A. Das,⁴² G. Davies,⁴⁰ S.J. de Jong,^{29,30} E. De La Cruz-Burelo,²⁸ F. Déliot,¹⁵ R. Demina,⁶³ D. Denisov,⁴⁵ S.P. Denisov,³⁴ S. Desai,⁴⁵ C. Deterre^c,²⁰ K. DeVaughan,⁵⁹ H.T. Diehl,⁴⁵ M. Diesburg,⁴⁵ P.F. Ding,⁴¹ A. Dominguez,⁵⁹ A. Dubey,²⁴ L.V. Dudko,³³ A. Duperrin,¹² S. Dutt,²³ M. Eads,⁴⁷ D. Edmunds,⁵⁷ J. Ellison,⁴³ V.D. Elvira,⁴⁵ Y. Enari,¹⁴ H. Evans,⁴⁹ V.N. Evdokimov,³⁴ L. Feng,⁴⁷ T. Ferbel,⁶³ F. Fiedler,²¹ F. Filthaut,^{29,30} W. Fisher,⁵⁷ H.E. Fisk,⁴⁵ M. Fortner,⁴⁷ H. Fox,³⁹ S. Fuess,⁴⁵ P.H. Garbincius,⁴⁵ A. Garcia-Bellido,⁶³ J.A. García-González,²⁸ V. Gavrilov,³² W. Geng,^{12,57} C.E. Gerber,⁴⁶ Y. Gershtein,⁶⁰ G. Ginther,^{45,63} G. Golovanov,³¹ P.D. Grannis,⁶⁴ S. Greder,¹⁶ H. Greenlee,⁴⁵ G. Grenier,¹⁷ Ph. Gris,¹⁰ J.-F. Grivaz,¹³ A. Grohsjean^c,¹⁵ S. Grünendahl,⁴⁵ M.W. Grünewald,²⁶ T. Guillemin,¹³ G. Gutierrez,⁴⁵ P. Gutierrez,⁶⁷ J. Haley,⁶⁸ L. Han,⁴ K. Harder,⁴¹ A. Harel,⁶³ J.M. Hauptman,⁵² J. Hays,⁴⁰ T. Head,⁴¹ T. Hebbeker,¹⁸ D. Hedin,⁴⁷ H. Hegab,⁶⁸ A.P. Heinson,⁴³ U. Heintz,⁶⁹ C. Hensel,¹ I. Heredia-De La Cruz^d,²⁸ K. Herner,⁴⁵ G. Hesketh^f,⁴¹ M.D. Hildreth,⁵¹ R. Hirosky,⁷³ T. Hoang,⁴⁴ J.D. Hobbs,⁶⁴ B. Hoeneisen,⁹ J. Hogan,⁷² M. Hohlfeld,²¹ J.L. Holzbauer,⁵⁸ I. Howley,⁷⁰ Z. Hubacek,^{7,15} V. Hynek,⁷ I. Iashvili,⁶² Y. Ilchenko,⁷¹ R. Illingworth,⁴⁵ A.S. Ito,⁴⁵ S. Jabeen,⁶⁹ M. Jaffré,¹³ A. Jayasinghe,⁶⁷ M.S. Jeong,²⁷ R. Jesik,⁴⁰ P. Jiang,⁴ K. Johns,⁴² E. Johnson,⁵⁷ M. Johnson,⁴⁵ A. Jonckheere,⁴⁵ P. Jonsson,⁴⁰ J. Joshi,⁴³ A.W. Jung,⁴⁵ A. Juste,³⁶ E. Kajfasz,¹² D. Karmanov,³³ I. Katsanos,⁵⁹ R. Kehoe,⁷¹ S. Kermiche,¹² N. Khalatyan,⁴⁵ A. Khanov,⁶⁸ A. Kharchilava,⁶² Y.N. Kharzheev,³¹ I. Kiselevich,³² J.M. Kohli,²³ A.V. Kozelov,³⁴ J. Kraus,⁵⁸ A. Kumar,⁶² A. Kupco,⁸ T. Kurča,¹⁷ V.A. Kuzmin,³³ S. Lammers,⁴⁹ P. Lebrun,¹⁷ H.S. Lee,²⁷ S.W. Lee,⁵² W.M. Lee,⁴⁵ X. Lei,⁴² J. Lellouch,¹⁴ D. Li,¹⁴ H. Li,⁷³ L. Li,⁴³ Q.Z. Li,⁴⁵ J.K. Lim,²⁷ D. Lincoln,⁴⁵ J. Linnemann,⁵⁷ V.V. Lipaev,³⁴ R. Lipton,⁴⁵ H. Liu,⁷¹ Y. Liu,⁴ A. Lobodenko,³⁵ M. Lokajicek,⁸ R. Lopes de Sa,⁶⁴ R. Luna-Garcia^g,²⁸ A.L. Lyon,⁴⁵ A.K.A. Maciel,¹ R. Madar,¹⁹ R. Magaña-Villalba,²⁸ S. Malik,⁵⁹ V.L. Malyshev,³¹ J. Mansour,²⁰ J. Martínez-Ortega,²⁸ R. McCarthy,⁶⁴ C.L. McGivern,⁴¹ M.M. Meijer,^{29,30} A. Melnitchouk,⁴⁵ D. Menezes,⁴⁷ P.G. Mercadante,³ M. Merkin,³³ A. Meyer,¹⁸ J. Meyerⁱ,²⁰ F. Miconi,¹⁶ N.K. Mondal,²⁵ M. Mulhearn,⁷³ E. Nagy,¹² M. Narain,⁶⁹ R. Nayyar,⁴² H.A. Neal,⁵⁶ J.P. Negret,⁵ P. Neustroev,³⁵ H.T. Nguyen,⁷³ T. Nunnemann,²² J. Orduna,⁷² N. Osman,¹² J. Osta,⁵¹ A. Pal,⁷⁰ N. Parashar,⁵⁰ V. Parihar,⁶⁹ S.K. Park,²⁷ R. Partridge^e,⁶⁹ N. Parua,⁴⁹ A. Patwa^j,⁶⁵ B. Penning,⁴⁵ M. Perfilov,³³ Y. Peters,⁴¹ K. Petridis,⁴¹ G. Petrillo,⁶³ P. Pétrouff,¹³ M.-A. Pleier,⁶⁵ V.M. Podstavkov,⁴⁵ A.V. Popov,³⁴ M. Prewitt,⁷² D. Price,⁴¹ N. Prokopenko,³⁴ J. Qian,⁵⁶ A. Quadt,²⁰ B. Quinn,⁵⁸ R. Raja,⁴⁵ P.N. Ratoff,³⁹ I. Razumov,³⁴ I. Ripp-Baudot,¹⁶ F. Rizatdinova,⁶⁸ M. Rominsky,⁴⁵ A. Ross,³⁹ C. Royon,¹⁵ P. Rubinov,⁴⁵ R. Ruchti,⁵¹ G. Sajot,¹¹ A. Sánchez-Hernández,²⁸ M.P. Sanders,²² A.S. Santos^h,¹ G. Savage,⁴⁵ L. Sawyer,⁵⁴ T. Scanlon,⁴⁰ R.D. Schamberger,⁶⁴ Y. Scheglov,³⁵ H. Schellman,⁴⁸ C. Schwanenberger,⁴¹ R. Schwienhorst,⁵⁷ J. Sekaric,⁵³ H. Severini,⁶⁷ E. Shabalina,²⁰ V. Shary,¹⁵ S. Shaw,⁵⁷ A.A. Shchukin,³⁴ V. Simak,⁷ P. Skubic,⁶⁷ P. Slattery,⁶³ D. Smirnov,⁵¹ G.R. Snow,⁵⁹ J. Snow,⁶⁶ S. Snyder,⁶⁵ S. Söldner-Rembold,⁴¹ L. Sonnenschein,¹⁸ K. Soustruznik,⁶ J. Stark,¹¹ D.A. Stoyanova,³⁴ M. Strauss,⁶⁷ L. Suter,⁴¹ P. Svoisky,⁶⁷ M. Titov,¹⁵ V.V. Tokmenin,³¹ Y.-T. Tsai,⁶³ D. Tsybychev,⁶⁴ B. Tuchming,¹⁵ C. Tully,⁶¹ L. Uvarov,³⁵ S. Uvarov,³⁵ S. Uzunyan,⁴⁷ R. Van Kooten,⁴⁹ W.M. van Leeuwen,²⁹ N. Varelas,⁴⁶ E.W. Varnes,⁴² I.A. Vasilyev,³⁴ A.Y. Verkheev,³¹ L.S. Vertogradov,³¹ M. Verzocchi,⁴⁵ M. Vesterinen,⁴¹ D. Vilanova,¹⁵ P. Vokac,⁷ H.D. Wahl,⁴⁴ M.H.L.S. Wang,⁴⁵ J. Warchol,⁵¹ G. Watts,⁷⁴ M. Wayne,⁵¹ J. Weichert,²¹ L. Welty-Rieger,⁴⁸ M.R.J. Williams,⁴⁹ G.W. Wilson,⁵³ M. Wobisch,⁵⁴ D.R. Wood,⁵⁵ T.R. Wyatt,⁴¹ Y. Xie,⁴⁵ R. Yamada,⁴⁵ S. Yang,⁴ T. Yasuda,⁴⁵ Y.A. Yatsunenkov,³¹ W. Ye,⁶⁴ Z. Ye,⁴⁵ H. Yin,⁴⁵ K. Yip,⁶⁵ S.W. Youn,⁴⁵ J.M. Yu,⁵⁶ J. Zennaro,⁶² T.G. Zhao,⁴¹ B. Zhou,⁵⁶ J. Zhu,⁵⁶ M. Zielinski,⁶³ D. Zieminska,⁴⁹ and L. Zivkovic¹⁴

(The D0 Collaboration*)

- ¹LAFEX, Centro Brasileiro de Pesquisas Físicas, Rio de Janeiro, Brazil
²Universidade do Estado do Rio de Janeiro, Rio de Janeiro, Brazil
³Universidade Federal do ABC, Santo André, Brazil
⁴University of Science and Technology of China, Hefei, People's Republic of China
⁵Universidad de los Andes, Bogotá, Colombia
⁶Charles University, Faculty of Mathematics and Physics, Center for Particle Physics, Prague, Czech Republic
⁷Czech Technical University in Prague, Prague, Czech Republic
⁸Institute of Physics, Academy of Sciences of the Czech Republic, Prague, Czech Republic
⁹Universidad San Francisco de Quito, Quito, Ecuador
¹⁰LPC, Université Blaise Pascal, CNRS/IN2P3, Clermont, France
¹¹LPSC, Université Joseph Fourier Grenoble 1, CNRS/IN2P3, Institut National Polytechnique de Grenoble, Grenoble, France
¹²CPPM, Aix-Marseille Université, CNRS/IN2P3, Marseille, France
¹³LAL, Université Paris-Sud, CNRS/IN2P3, Orsay, France
¹⁴LPNHE, Universités Paris VI and VII, CNRS/IN2P3, Paris, France
¹⁵CEA, Irfu, SPP, Saclay, France
¹⁶IPHC, Université de Strasbourg, CNRS/IN2P3, Strasbourg, France
¹⁷IPNL, Université Lyon 1, CNRS/IN2P3, Villeurbanne, France and Université de Lyon, Lyon, France
¹⁸III. Physikalisches Institut A, RWTH Aachen University, Aachen, Germany
¹⁹Physikalisches Institut, Universität Freiburg, Freiburg, Germany
²⁰II. Physikalisches Institut, Georg-August-Universität Göttingen, Göttingen, Germany
²¹Institut für Physik, Universität Mainz, Mainz, Germany
²²Ludwig-Maximilians-Universität München, München, Germany
²³Panjab University, Chandigarh, India
²⁴Delhi University, Delhi, India
²⁵Tata Institute of Fundamental Research, Mumbai, India
²⁶University College Dublin, Dublin, Ireland
²⁷Korea Detector Laboratory, Korea University, Seoul, Korea
²⁸CINVESTAV, Mexico City, Mexico
²⁹Nikhef, Science Park, Amsterdam, the Netherlands
³⁰Radboud University Nijmegen, Nijmegen, the Netherlands
³¹Joint Institute for Nuclear Research, Dubna, Russia
³²Institute for Theoretical and Experimental Physics, Moscow, Russia
³³Moscow State University, Moscow, Russia
³⁴Institute for High Energy Physics, Protvino, Russia
³⁵Petersburg Nuclear Physics Institute, St. Petersburg, Russia
³⁶Institució Catalana de Recerca i Estudis Avançats (ICREA) and Institut de Física d'Altes Energies (IFAE), Barcelona, Spain
³⁷Uppsala University, Uppsala, Sweden
³⁸Taras Shevchenko National University of Kyiv, Kiev, Ukraine
³⁹Lancaster University, Lancaster LA1 4YB, United Kingdom
⁴⁰Imperial College London, London SW7 2AZ, United Kingdom
⁴¹The University of Manchester, Manchester M13 9PL, United Kingdom
⁴²University of Arizona, Tucson, Arizona 85721, USA
⁴³University of California Riverside, Riverside, California 92521, USA
⁴⁴Florida State University, Tallahassee, Florida 32306, USA
⁴⁵Fermi National Accelerator Laboratory, Batavia, Illinois 60510, USA
⁴⁶University of Illinois at Chicago, Chicago, Illinois 60607, USA
⁴⁷Northern Illinois University, DeKalb, Illinois 60115, USA
⁴⁸Northwestern University, Evanston, Illinois 60208, USA
⁴⁹Indiana University, Bloomington, Indiana 47405, USA
⁵⁰Purdue University Calumet, Hammond, Indiana 46323, USA
⁵¹University of Notre Dame, Notre Dame, Indiana 46556, USA
⁵²Iowa State University, Ames, Iowa 50011, USA
⁵³University of Kansas, Lawrence, Kansas 66045, USA
⁵⁴Louisiana Tech University, Ruston, Louisiana 71272, USA
⁵⁵Northeastern University, Boston, Massachusetts 02115, USA
⁵⁶University of Michigan, Ann Arbor, Michigan 48109, USA
⁵⁷Michigan State University, East Lansing, Michigan 48824, USA
⁵⁸University of Mississippi, University, Mississippi 38677, USA
⁵⁹University of Nebraska, Lincoln, Nebraska 68588, USA
⁶⁰Rutgers University, Piscataway, New Jersey 08855, USA

- ⁶¹Princeton University, Princeton, New Jersey 08544, USA
⁶²State University of New York, Buffalo, New York 14260, USA
⁶³University of Rochester, Rochester, New York 14627, USA
⁶⁴State University of New York, Stony Brook, New York 11794, USA
⁶⁵Brookhaven National Laboratory, Upton, New York 11973, USA
⁶⁶Langston University, Langston, Oklahoma 73050, USA
⁶⁷University of Oklahoma, Norman, Oklahoma 73019, USA
⁶⁸Oklahoma State University, Stillwater, Oklahoma 74078, USA
⁶⁹Brown University, Providence, Rhode Island 02912, USA
⁷⁰University of Texas, Arlington, Texas 76019, USA
⁷¹Southern Methodist University, Dallas, Texas 75275, USA
⁷²Rice University, Houston, Texas 77005, USA
⁷³University of Virginia, Charlottesville, Virginia 22904, USA
⁷⁴University of Washington, Seattle, Washington 98195, USA

(Dated: April 6, 2014)

The electron and photon reconstruction and identification algorithms used by the D0 Collaboration at the Fermilab Tevatron collider are described. The determination of the electron energy scale and resolution is presented. Studies of the performance of the electron and photon reconstruction and identification are summarized. The results are based on measurements of Z boson decay events of $Z \rightarrow ee$ and $Z \rightarrow \gamma\ell\ell$ ($\ell = e, \mu$) collected in $p\bar{p}$ collisions at a center-of-mass energy of 1.96 TeV using an integrated luminosity of up to 10 fb^{-1} .

PACS numbers:

I. INTRODUCTION

The precise and efficient reconstruction and identification of electrons¹ and photons at the D0 experiment at the Fermilab Tevatron $p\bar{p}$ collider is essential for a broad spectrum of physics analyses, including high precision standard model (SM) measurements and searches for new phenomena. To satisfy this requirement, the D0 detector was designed to have excellent performance for the measurements of electrons and photons of energies from a few GeV up to $\mathcal{O}(100 \text{ GeV})$. Another design requirement was to have good discrimination between jets and electrons or photons, since physics measurements often suffer from large backgrounds induced by jets being misidentified as electrons or photons. In this paper, the reconstruction of electromagnetic (EM) objects using D0 data is described. The determination of the electron energy scale and resolution and the performance of electron and photon identification using the Run II dataset recorded between 2002 and 2011 are presented.

II. D0 DETECTOR

The D0 detector is described elsewhere [1]. The components most relevant to electron and photon identification are the central tracking system, composed of a silicon microstrip tracker (SMT) that is located near the $p\bar{p}$ interaction point and a central fiber tracker (CFT) embedded in a 2 T solenoidal magnetic field, a central preshower (CPS), and a liquid-argon/uranium sampling calorimeter. The CPS is located before the inner layer of the calorimeter, outside the calorimeter cryostat, and is formed of one radiation length of absorber followed by three layers of scintillating strips. The D0 coordinate system is right-handed. The z -axis points in the direction of the Tevatron proton beam, and the y -axis points upwards. Pseudorapidity is defined as $\eta = -\ln[\tan(\theta/2)]$, where θ is the polar angle relative to the proton beam direction. The azimuthal angle ϕ is defined in the plane transverse to the proton beam direction. The SMT covers $|\eta| < 3$, and the CFT provides complete coverage out to $|\eta| \approx 1.7$.

The calorimeter consists of a central section (CC) with coverage in pseudorapidity of $|\eta| < 1.1$, and two endcap calorimeters (EC) covering up to $|\eta| \approx 4.2$, as shown in Fig. 1. The region $1.1 < |\eta| < 1.5$ is not fully covered by the calorimeter. Therefore, the reconstruction, identification, energy scale and resolution estimation methods described in the paper can not be used. In that particular region, the tracking system is mainly used for reconstruction which is beyond the scope of this paper. Each part of the calorimeter is contained in its own cryostat and comprises an EM section, closest to the interaction region, and a hadronic section. The EM section of the calorimeter is segmented into four longitudinal layers with transverse segmentation of $\Delta\eta \times \Delta\phi = 0.1 \times 0.1$, except in the

*with visitors from ^aAugustana College, Sioux Falls, SD, USA, ^bThe University of Liverpool, Liverpool, UK, ^cDESY, Hamburg, Germany, ^dUniversidad Michoacana de San Nicolas de Hidalgo, Morelia, Mexico ^eSLAC, Menlo Park, CA, USA, ^fUniversity College London, London, UK, ^gCentro de Investigacion en Computacion - IPN, Mexico City, Mexico, ^hUniversidade Estadual Paulista, São Paulo, Brazil, ⁱKarlsruher Institut für Technologie (KIT) - Steinbuch Centre for Computing (SCC), D-76128 Karlsruhe, Germany, ^jOffice of Science, U.S. Department of Energy, Washington, D.C. 20585, USA, ^kAmerican Association for the Advancement of Science, Washington, D.C. 20005, USA and ^lKiev Institute for Nuclear Research, Kiev, Ukraine

¹ In the following, if not indicated otherwise, “electron” denotes both electrons and positrons.

third layer (EM3), where the segmentation is 0.05×0.05 . There are 32 azimuthal modules for EM layers in the CC. The hadronic section is composed of fine (FH) and coarse (CH) layers. The FH layers are closer to the interaction point, followed by the CH layers.

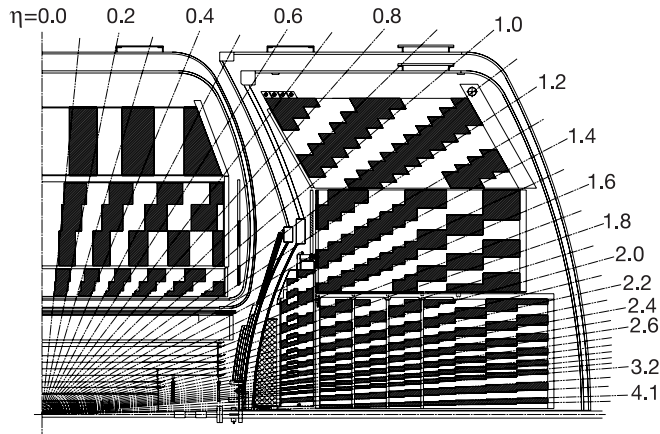


FIG. 1: Side view of a quadrant of the D0 calorimeters showing the transverse and longitudinal segmentation. The alternating shading pattern indicates the cells for signal readout. The lines indicate the pseudorapidity intervals defined from the center of the detector. The CC covers the region $|\eta| < 1.1$ and the EC extends the coverage to $|\eta| \approx 4.2$.

There is material varying between 3.4 and 5 radiation lengths (X_0) between the beam line and the CC. For EC, it varies between 1.8 and $4.8 X_0$. The amount of material depends on the incident angle of the electron or photon [2]. At $\eta \approx 0$, the amount of material in front of the calorimeter is $0.2 X_0$ in the tracking detector, $0.9 X_0$ in the solenoid, $0.3 X_0$ in the preshower detector plus $1.0 X_0$ in the associated lead, and $1.3 X_0$ in the cryostat walls plus related support structures.

III. DATA AND MONTE CARLO SAMPLES

Data and Monte Carlo (MC) simulated events have been used to study reconstruction and identification efficiencies, to measure the energy scale and resolution, and to derive correction factors to compensate for any residual mismodelling of the detector. The electron candidates are selected from $Z \rightarrow ee$ data and MC using the “tag-and-probe method” as described in Sect. VII A. The photon candidates are selected from diphoton MC and $Z \rightarrow \gamma\ell\ell$ ($\ell = e, \mu$) data and MC, where the photons are radiated from charged leptons in Z boson decays by requiring the dilepton invariant mass to be less than 82 GeV while the three-body mass of dilepton and photon $M_{\ell\ell\gamma}$ is required to be $82 < M_{\ell\ell\gamma} < 102$ GeV [3]. To evaluate misidentification of jets as electrons or photons, dijet events are selected. For dijet MC, an EM cluster

passing the preselection as described in Sect. IV A is selected as jets misidentified as electrons or photons. For dijet data, a jet [4] with transverse momentum $p_T > 20$ GeV and $|\eta| < 2.5$ is selected, then a preselected EM cluster is selected in the opposite azimuthal plane with $|\Delta\phi(\text{jet}, \text{EM})| > 2.9$ radian as the jets misidentified as electrons or photons. To eliminate possible contamination from diboson, $Z + \text{jets}$ and $W + \text{jets}$ processes, events with at least one isolated high- p_T muon [5], events with an invariant mass of the EM cluster and an isolated track between 60 and 120 GeV, and events with missing transverse energy [6] greater than 10 GeV are rejected. For studies of jets misidentified as photons, the $\gamma + \text{jet}$ component containing a real photon is removed from the dijet sample by requiring that the EM cluster be non-isolated by cutting on the shower isolation fraction (see Sect. IV A) of $0.07 < f_{\text{iso}} < 0.15$. The $Z \rightarrow ee$ and $Z \rightarrow ee\gamma$ data events are collected using single electron triggers as described in Sect. VII B. For $Z \rightarrow \mu\mu\gamma$ and dijet data events, single muon triggers [5] and jet triggers [4] are used, respectively.

The data used in physics analyses were collected by the D0 detector during Tevatron Run II between April 2002 and September 2011 and correspond to an integrated luminosity of approximately 10 fb^{-1} .

The $Z \rightarrow ee$ signal samples are generated using the ALPGEN generator [7] interfaced to PYTHIA [8] for parton showering and hadronization. The simulated transverse momentum p_T distribution of the Z boson is weighted to match the distribution observed in data [9]. Diphoton and $Z \rightarrow \gamma\ell\ell$ ($\ell = e, \mu$) signal events, and dijet background samples are generated using PYTHIA [8]. All MC samples used here are generated using the CTEQ6L1 [10] parton distribution functions, followed by a GEANT [11] simulation of the D0 detector. To accurately model the effects of multiple $p\bar{p}$ interactions in a single bunch crossing and detector noise, data from random $p\bar{p}$ bunch crossings are overlaid on the MC events. The instantaneous luminosity spectrum of these overlaid events is matched to that of the events used in the data analysis. Simulated events are processed using the same reconstruction code that is used for data.

IV. EM OBJECT RECONSTRUCTION AND IDENTIFICATION

EM objects – electrons and photons – are reconstructed by detecting localized energy deposits in the EM calorimeter. Confirmation of the existence of an electron track is sought from the central tracking system since an isolated high- p_T track should originate from the interaction vertex. The hadronic calorimeter, preshower, and tracking systems can be used to differentiate electrons and photons from jets.

A. EM cluster reconstruction

EM objects in the D0 detector are reconstructed using the nearly 55,000 calorimeter channels. Only channels with energies above noise are read out [4]. We use the same cluster reconstruction algorithm for electrons and photons, since their showers both consist of collimated clusters of energy deposited mainly in the EM layers of the calorimeter. Calorimeter cells with the same η and ϕ are grouped together to form towers. For the calculation of the energy of EM clusters, we sum the energies measured in the four EM layers and the first hadronic (FH1) layer which is included to account for leakage of energy of EM objects into the hadronic part of the calorimeter. Starting with the highest transverse energy tower ($E_T > 500$ MeV), energies of adjacent towers in a cone of radius $\mathcal{R} = \sqrt{(\Delta\eta)^2 + (\Delta\phi)^2} = 0.4$ around the highest E_T tower are added to form EM clusters in the CC². In the EC, EM clusters are a set of adjacent cells with a transverse distance of less than 10 cm from an initial cell with the highest energy content in the EM3 layer.

To be selected as an EM candidate, EM clusters must satisfy the following set of criteria:

- The cluster transverse energy must be $E_T > 1.5$ GeV.
- The fraction of energy in the EM layers is

$$f_{\text{EM}} = \frac{E_{\text{EM}}}{E_{\text{tot}}}, \quad (1)$$

where E_{EM} is the cluster energy in the EM layers, and E_{tot} is the total energy of the cluster in all layers within the cone. At least 90% of the energy should be deposited in the EM layers of the calorimeter.

- The isolation fraction is the ratio of the energy in an isolation cone surrounding an EM cluster to the energy of the EM cluster,

$$f_{\text{iso}} = \frac{E_{\text{tot}}(\mathcal{R} < 0.4) - E_{\text{EM}}(\mathcal{R} < 0.2)}{E_{\text{EM}}(\mathcal{R} < 0.2)}, \quad (2)$$

where $E_{\text{tot}}(\mathcal{R} < 0.4)$ is the total energy within a cone of radius $\mathcal{R} = 0.4$ around the cluster, summed over the entire depth of the calorimeter except the CH layers, and $E_{\text{EM}}(\mathcal{R} < 0.2)$ is the energy in the towers in a cone of radius $\mathcal{R} = 0.2$ summed over the EM layers only. To select isolated electron or

photon clusters in the calorimeter, we require an isolation fraction of less than 0.2.

For each EM candidate, the centroid of the EM cluster is computed by weighting cell coordinates with cell energies in the EM3 layer of the calorimeter. The shower centroid position together with the location of the $p\bar{p}$ collision vertex is used to calculate the direction of the EM object momentum.

Since EM objects begin to shower in the preshower detector, clusters are also formed in that detector. Single layer clusters are formed from scintillating strips for each layer. A preshower cluster is built by combining the single layer clusters from each of the three layers. These preshower clusters are extensively used to help identify the electrons and photons, and to build the multivariate identification methods, as well as to find the right interaction vertex for the photon as described in the following sections.

Electron candidates are distinguished from photon candidates by the presence of a track with $p_T > 1.5$ GeV within a window of $\Delta\eta \times \Delta\phi = 0.05 \times 0.05$ around the coordinates of the EM cluster. The momentum of an electron candidate is recalculated using the direction of the best spatially matched track while the energy of the electron is measured by the calorimeter due to limited momentum resolution of the central tracking system. An EM cluster is considered to be a photon candidate if there is no associated track.

B. EM object identification

After applying the above criteria to EM clusters, there remains a considerable fraction of jets misidentified as EM objects. Further criteria must be applied to reject these misidentified jets and increase the purity of the selected electron and photon candidates. The following is a description of the quantities employed for electron and photon identification. There are a number of different selection criteria for these quantities to meet the needs of different physics analyses.

a. EM energy fraction Because the development of EM and hadronic showers are substantially different, shower shape information can be used to differentiate between electrons, photons, and hadrons. Electrons and photons deposit almost all their energy in the EM section of the calorimeter while hadrons are typically much more penetrating. EM clusters typically have a large EM fraction, f_{EM} (Eq. 1). The requirement of large values of f_{EM} is very efficient for rejecting hadrons, but also removes electrons pointing to the module boundaries (in ϕ) of the central EM calorimeter, since they deposit a considerable fraction of their energy in the hadronic calorimeter.

b. EM shower isolation Electrons and photons from a prompt decay of W and Z bosons tend to be isolated in the calorimeter, and therefore usually have a low isolation fraction f_{iso} (Eq. 2). In this case most of the energy of

² We use the terms ‘‘CC EM cluster’’ to denote EM clusters in the pseudorapidity range $|\eta| < 1.1$, and ‘‘EC EM cluster’’ to denote EM clusters in the pseudorapidity range $1.5 < |\eta| < 3.2$.

the EM cluster is deposited in a narrow cone of radius $\mathcal{R} = 0.2$ in the calorimeter.

c. EM shower width Showers induced by electrons and photons are usually narrower than those from jets. The EM3 layer of the calorimeter has a fine segmentation, providing sensitive variables to separate electrons and photons from misidentified jets. The squared width, σ_ϕ^2 , of the shower shape in the transverse plane is calculated as

$$\sigma_\phi^2 = \frac{\sum (5.5 + \log \left(\frac{E_{\text{cell}}^i}{E_{\text{EM3}}} \right)) \cdot (r_{\text{cell}}^i \times \sin(\phi_{\text{cell}}^i - \phi_{\text{EM}}))^2}{\sum (5.5 + \log \left(\frac{E_{\text{cell}}^i}{E_{\text{EM3}}} \right))}, \quad (3)$$

where E_{cell}^i , r_{cell}^i and ϕ_{cell}^i are the energy, radius calculated from z -axis and azimuthal angle for cell i in the EM3 layer associated to the EM cluster, and E_{EM3} and ϕ_{EM} are the total energy and centroid azimuthal angle of the EM cluster at the EM3 layer. A value of 5.5 was chosen as a result of studies to eliminate effect of low energy cells. Only the cells with positive weight $(5.5 + \log \left(\frac{E_{\text{cell}}^i}{E_{\text{EM3}}} \right)) > 0$ are used in the calculation. The width σ_η of the shower in the pseudorapidity direction is calculated as

$$\sigma_\eta = \sqrt{\frac{\sum (5.5 + \log \left(\frac{E_{\text{cell}}^i}{E_{\text{EM3}}} \right)) \cdot \eta_i^2}{\sum (5.5 + \log \left(\frac{E_{\text{cell}}^i}{E_{\text{EM3}}} \right))} - \left(\frac{\sum (5.5 + \log \left(\frac{E_{\text{cell}}^i}{E_{\text{EM3}}} \right)) \cdot \eta_i}{\sum (5.5 + \log \left(\frac{E_{\text{cell}}^i}{E_{\text{EM3}}} \right))} \right)^2}, \quad (4)$$

where E_{cell}^i and η_i are the energy and pseudorapidity of cell i .

d. H-matrix technique The shower shape of an electron or a photon is distinct from that of a jet. Fluctuations cause the energy deposition to vary from the average in a correlated fashion among the cells and layers. Longitudinal and transverse shower shapes, and the correlations between energy depositions in the calorimeter cells are taken into account to obtain the best discrimination against hadrons, using a covariance matrix (“H-matrix”) technique [12, 13]. A covariance matrix is formed from a set of eight well-modeled variables describing shower shapes:

- The longitudinal development is described by the fractions of shower energy in the four EM layers (EM1, EM2, EM3, EM4).
- To characterize the lateral development of the shower, we consider the shower width in both dimensions in the third EM layer (σ_ϕ^2 and σ_η), which is the layer with the finest granularity. The logarithm of the total shower energy and the coordinate of the $p\bar{p}$ collision vertex along the beam axis are included, so that the dependence of the H-matrix on these quantities is properly parametrized.

In the EC the matrix is of dimension 8×8 , while in the CC σ_η is not used and therefore the matrix has the

dimension 7×7 . A separate matrix is built for each ring of calorimeter cells with the same $|\eta|$ coordinate. To measure how closely the shower shape of an electron candidate matches expectations from MC simulations, a χ^2 value is calculated (χ_{Cal}^2). Since the electron and photon candidates tend to have smaller χ_{Cal}^2 than jets, this variable can be used to discriminate between EM and hadronic showers.

e. Track isolation For electrons and photons that are isolated, the scalar sum of the p_T of all charged particle tracks with $p_T > 0.5$ GeV, excluding the associated track for the EM cluster, originating from the $p\bar{p}$ collision vertex in an annular cone of $0.05 < \mathcal{R} < 0.4$ around the electron and photon candidates, Σp_T^{trk} , is expected to be small. It is therefore a sensitive variable for discriminating between EM objects and jets.

f. Track match For electron identification, to suppress photons and jets misidentified as electrons, the cluster is required to be associated with a track in the central tracking system in a road between the EM calorimeter cluster and the $p\bar{p}$ collision vertex satisfying the conditions $|\Delta\eta_{\text{EM, trk}}| < 0.05$ and $|\Delta\phi_{\text{EM, trk}}| < 0.05$ for the differences between η and ϕ of the EM cluster and the associated track. To quantify the quality of the cluster-track matching, a matching probability $P(\chi_{\text{spatial}}^2)$ is defined using χ_{spatial}^2 , which is given by

$$\chi_{\text{spatial}}^2 = \left(\frac{\Delta\phi}{\delta_\phi} \right)^2 + \left(\frac{\Delta\eta}{\delta_\eta} \right)^2. \quad (5)$$

The probability is computed for each matched track. In these expressions, $\Delta\eta$ and $\Delta\phi$ are the differences between the track position and the EM cluster position in the EM3 layer of the calorimeter. The variables δ_ϕ and δ_η are the resolutions of the associated quantities. The track with the highest $P(\chi_{\text{spatial}}^2)$ is taken to be the track matched to the EM object. If there is no matched track, $P(\chi_{\text{spatial}}^2)$ is set to -1 .

g. Hits on road Due to tracking inefficiencies, the cluster-track matching probability method is not fully efficient in separating electron from photon candidates, in particular in events with high instantaneous luminosity. To improve the separation between electron and photon candidates, a “hits on road” discriminant, D_{hor} , is used in the CC. For each EM object, a “road” is defined between the $p\bar{p}$ collision vertex position and the CPS cluster position, if it is matched to the EM object, or else to the EM cluster position. To account for the different sign of the electric charge of electrons and positrons, two roads (positive-charge and negative-charge roads) are defined. The number of hits from CFT fibers and SMT strips along the EM cluster’s trajectory, N_{hits} , is counted. The discriminant D_{hor} is defined by

$$D_{\text{hor}} = \frac{P_e(N_{\text{hits}})}{P_e(N_{\text{hits}}) + P_\gamma(N_{\text{hits}})}, \quad (6)$$

where P_e and P_γ are the probabilities in the bin of N_{hits} , given by

$$P_e(N_{\text{hits}}) = \frac{\sum_{i=0}^{N_{\text{hits}}} N_e^i}{\sum_{i=0}^{24} N_e^i}, \quad (7)$$

$$P_\gamma(N_{\text{hits}}) = \frac{\sum_{i=N_{\text{hits}}}^{24} N_f^i}{\sum_{i=0}^{24} N_f^i}, \quad (8)$$

where N_e^i and N_f^i are the number of electrons and fake electrons in the bin $N_{\text{hits}} = i$ from $Z \rightarrow ee$ and multijet data events, respectively. The maximum number of hits is 24, as the maximum of CFT hits is 16 and the maximum of SMT hits is 8. Electrons tend to have $D_{\text{hor}} \approx 1$, while photons tend to have values close to 0.

Figs. 2-4 show distributions of identification variables for EM candidates from $Z \rightarrow ee$ data and MC events, as well as from diphoton and dijet MC events³. As can be inferred from the distributions, the simulation has some imperfections in modeling the shower shapes mainly caused by an insufficient description of uninstrumented material [2]. This is accounted for when correcting simulated electron and photon identification efficiencies utilizing data as described in Sects. VII and VIII, respectively.

V. MULTIVARIATE IDENTIFICATION METHODS

The variables described in Sect. IV B allow efficient identification of electron and photon candidates. However, to maximize the identification efficiencies of electrons and photons and to minimize the misidentification rate from jets in physics analyses, various multivariate analysis (MVA) techniques are explored. One MVA technique, the H-matrix method, has already been discussed in Sect. IV B 0 d. Two more types of MVAs that are used in physics analyses are a Likelihood method for electrons and a neural network (NN) method for electrons and photons. H-matrix, Likelihood, and NN achieve an improved background rejection. However, the H-matrix is mainly based on the calorimeter information, while the Likelihood method includes the tracking information in addition, while the advantage of the NN is that it includes CPS information. The electron identification efficiency and purity are therefore found to be improved when these MVA output variables are utilized together with other electron reconstruction variables as input to

a Boosted Decision Tree (BDT) [14]. All MVAs except the H-matrix are described in this section.

A. Electron Likelihood

Likelihood-based identification of electron candidates is an efficient technique for separating electrons from background by combining information from various detector components into a single discriminant.

There are several mechanisms by which particles, either isolated or in jets, may produce electron signatures. Photon conversions may be marked by the presence of a track very close to the track matched to the EM cluster, or a large E_T/p_T when the closely situated ee pair is reconstructed as a single EM cluster and only one track is identified. Here, E_T is the transverse energy of the cluster measured by the calorimeter and p_T is the transverse momentum of the associated track measured by the tracker. The calorimeter quantities describing the shower shape, however, are nearly identical to that of an electron, though photon calorimeter clusters may be slightly wider than an electron shower. Neutral pions (π^0) may also have nearby tracks, as they are generally produced in association with other charged hadrons. Since the $\pi^0 \rightarrow \gamma\gamma$ decay would have to overlap with a charged hadron track in order to fake an electron, the track matching quantity could be poor, and the track would not necessarily be isolated. The H-matrix χ_{Cal}^2 and f_{EM} of the EM object may be influenced by the surrounding hadrons. The following eight variables are used to calculate the electron likelihood⁴:

- EM energy fraction f_{EM} ;
- EM shower isolation f_{iso} ;
- H-matrix χ_{Cal}^2 ;
- E_T/p_T ;
- transverse impact parameter of the selected track with respect to the $p\bar{p}$ collision vertex;
- number of tracks with $p_T > 0.5$ GeV in a cone of radius $\mathcal{R} = 0.4$ around and including the matched track;
- cluster-track matching probability $P(\chi_{\text{spatial}}^2)$;
- track isolation variable Σp_T^{trk} .

The distributions of these eight variables are normalized to unit area to generate probability density distributions for each variable from $Z \rightarrow ee$ and dijet data for signal and background, respectively. These distributions are used to assign a probability for a given EM object

³ The distributions shown in this paper are generally derived from subsets of the Run II data sample. The small variations observed between different periods of Run II are treated as systematic uncertainties in physics analyses.

⁴ For definitions see Sect. IV.

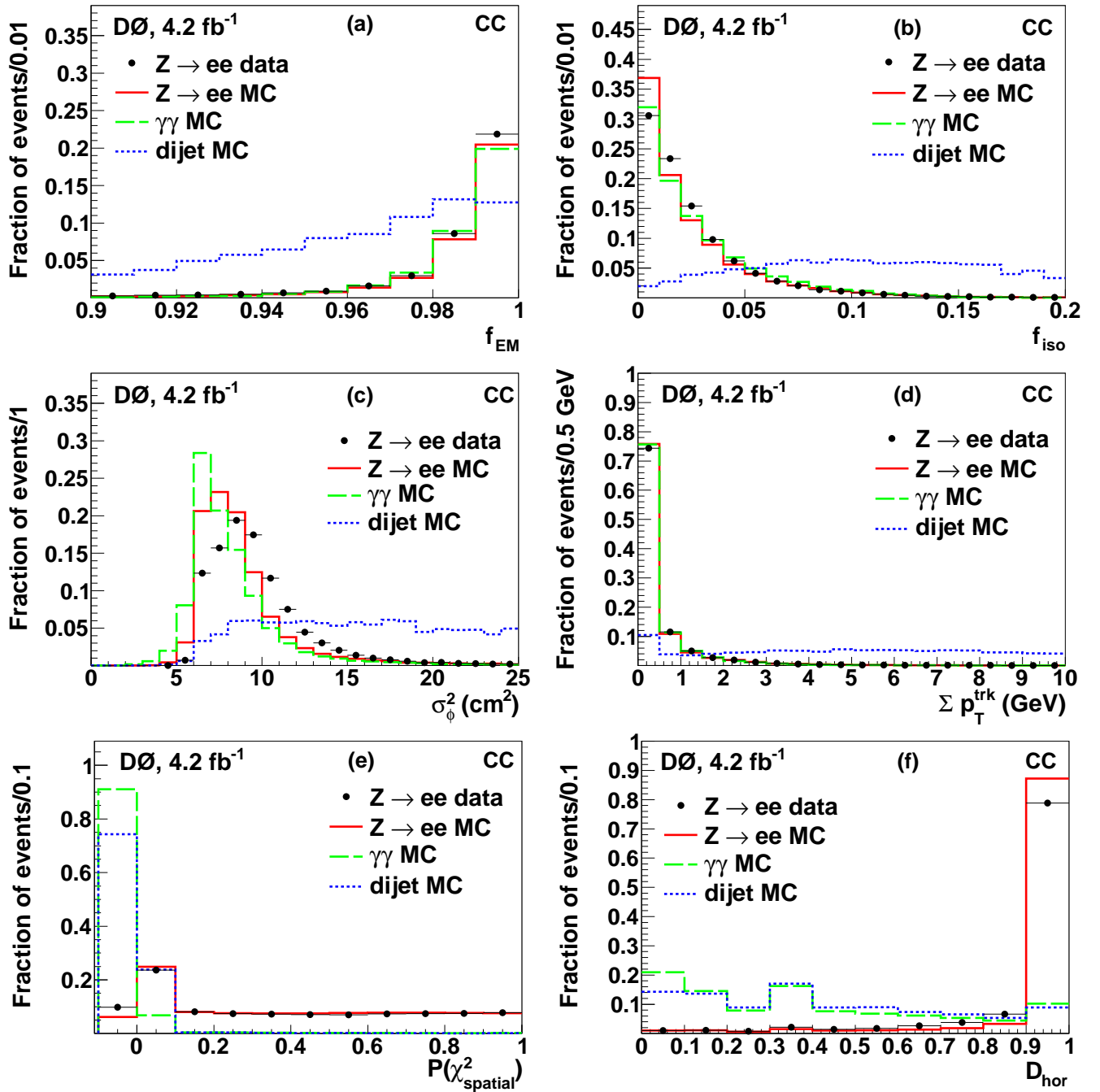


FIG. 2: Normalized distributions of EM object identification variables as defined in Sect. IV B for $Z \rightarrow ee$ data and MC events, and for diphoton and dijet MC events in the CC. Presented are (a) the EM energy fraction, (b) the EM shower isolation, (c) the width of the EM shower in the transverse plane, (d) the track isolation, (e) the track matching probability, and (f) the hits on road discriminant. The first bin of the track matching probability distribution indicates no track match.

to be signal or background. To quantify the degree of correlation between the input variables, we calculate the correlation coefficients. We find that most of the combinations have correlation coefficients close to zero and hence are mutually uncorrelated. Others do not exceed 55% for signal or fake electrons. The product of individual probabilities from all variables is correlated with the

overall probability for the EM object to be an electron. To differentiate between signal-like and background-like electron candidates, a likelihood discriminant is calculated:

$$\mathcal{L} = \frac{P_{\text{sig}}}{P_{\text{sig}} + P_{\text{bkg}}}, \quad (9)$$

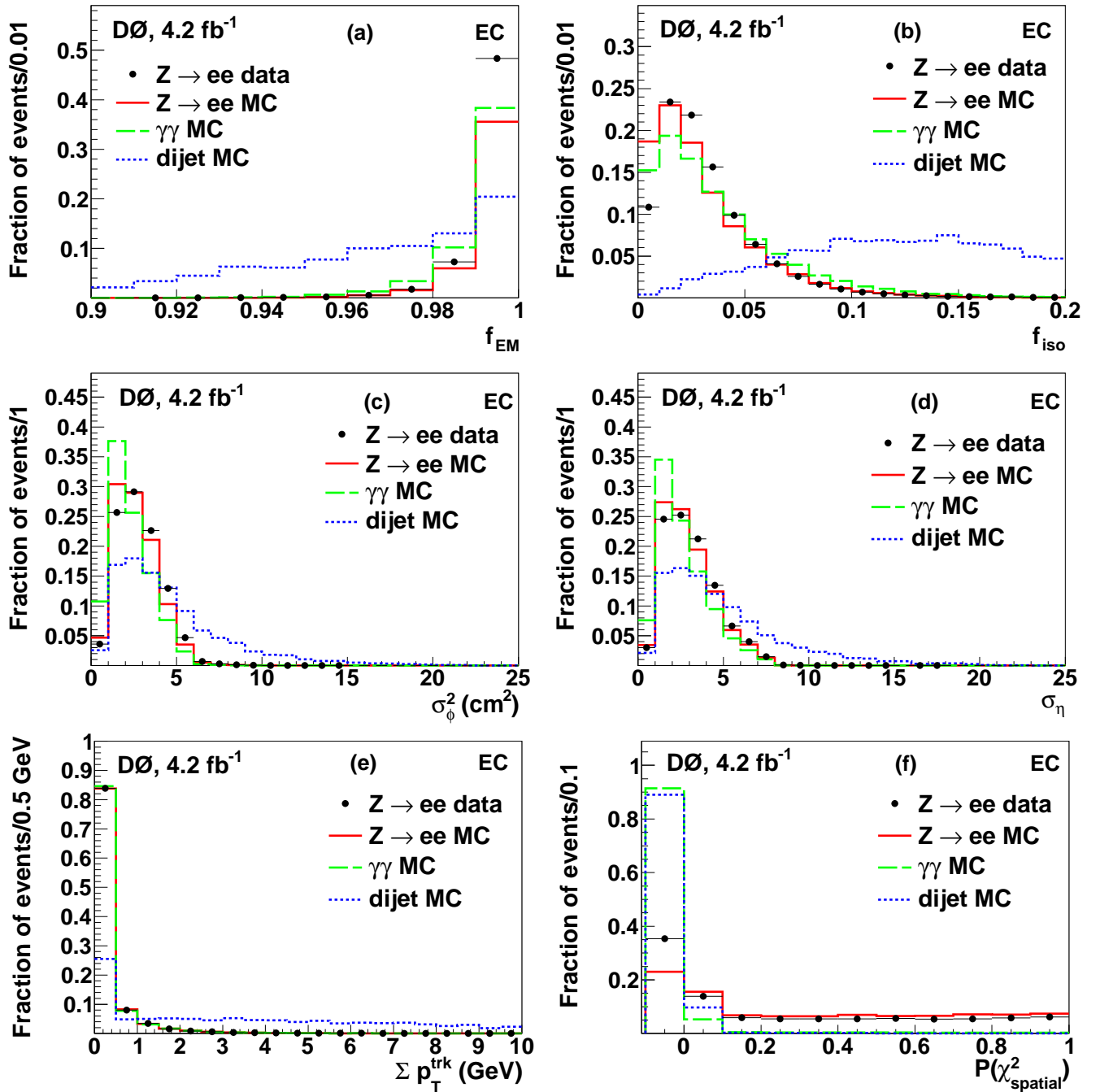


FIG. 3: Normalized distributions of EM object identification variables as defined in Sect. IV B for $Z \rightarrow ee$ data and MC events, and for diphoton and dijet MC events in the EC. Presented are (a) the EM energy fraction, (b) the EM shower isolation, (c) the width of the EM shower in the transverse plane, (d) the width of the EM shower in the pseudorapidity direction, (e) the track isolation, and (f) the track matching probability. The first bin of the track matching probability distribution indicates no track match.

where P_{sig} and P_{bkg} are the overall probabilities for signal and background, respectively. Distributions of this discriminant for electron candidates in the CC and EC are presented in Fig. 5. This demonstrates the enhanced power to separate between genuine electrons, which peak at large values of the discriminant, and jets, which peak

at low values.

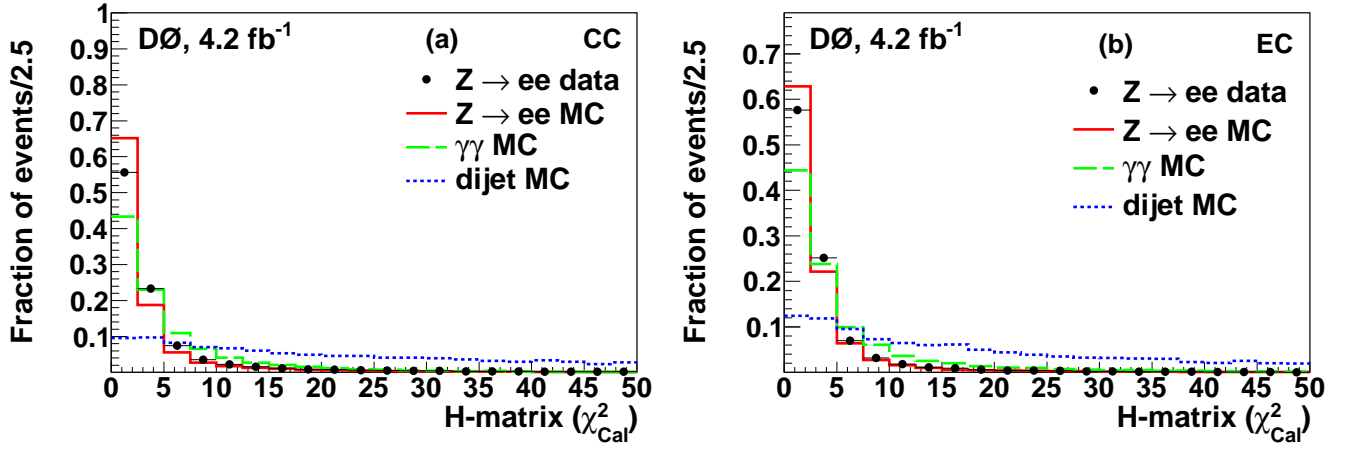


FIG. 4: The distributions of χ_{Cal}^2 for EM candidates for $Z \rightarrow ee$ data and MC events, and for diphoton and dijet MC events in the CC (a) and EC (b).

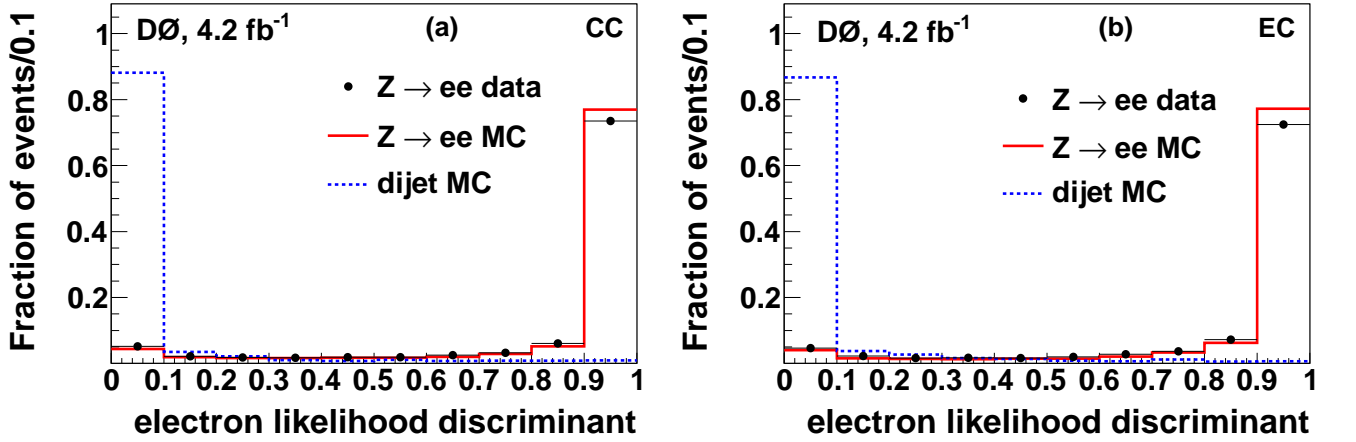


FIG. 5: Distribution of the electron likelihood discriminant of electron candidates in $Z \rightarrow ee$ data and MC events, and in dijet MC events in the CC (a) and EC (b).

B. Neural Network for electron and photon identification

To further suppress jets misidentified as electrons and photons, we train an NN [15] using a set of variables that are sensitive to differences between electrons (photons) and jets. The variables, selected to explore both the tracker activity and the energy distribution in the calorimeter and CPS, are listed below.

- fraction of the EM cluster energy deposited in the first EM calorimeter layer (f_{EM1});
- number of cells above an EM cluster E_T -dependent threshold, given by $0.004 \times E_T$ (in GeV) + 0.25 GeV in the first EM calorimeter layer within $\mathcal{R} < 0.2$ ($N_{\text{cells}}^{\mathcal{R} < 0.2}$) and $0.2 < \mathcal{R} < 0.4$ ($N_{\text{cells}}^{0.2 < \mathcal{R} < 0.4}$) of the EM cluster;
- track isolation variable Σp_T^{trk} ;

- number of charged particle tracks with $p_T > 0.5$ GeV originating from the $p\bar{p}$ collision vertex within $\mathcal{R} < 0.05$ of the EM cluster ($N_{\text{trks}}^{\mathcal{R} < 0.05}$);
- number of CPS clusters within $\mathcal{R} < 0.1$ of the EM cluster (N_{cps});
- squared width of the energy deposit in the CPS:

$$\sigma_{\text{CPS}}^2 = \frac{\sum_i E_i^2 \times (\phi_{\text{EM}} - \phi_i)^2}{\sum_i E_i^2}, \quad (10)$$

where E_i and ϕ_i are the energy and azimuthal angle of the i^{th} strip in CPS in the direction of the EM cluster and ϕ_{EM} is the azimuthal angle of the EM cluster at the EM3 layer;

- χ_{Cal}^2 calculated from the H-matrix.

Separate NNs are built for electrons and photons in the CC, whereas a single NN is used for electrons and photons

in the EC. Table I lists the input variables utilized in each NN.

For the construction of the NN for electrons in the CC, the seven variables above are used as inputs (e NN7). Here, $Z \rightarrow ee$ data events define the signal, and dijet data events define the background. Performance checks have been performed using $Z \rightarrow ee$ and dijet MC events.

The NN for CC photons (γ NN5) is built from the same variables as e NN7 but excluding the tracker-based variable $N_{\text{trks}}^{\mathcal{R} < 0.05}$, and f_{EM1} since its distribution varies significantly with the E_T of the EM cluster. The direct diphoton MC defines the signal, and dijet MC events are used as background in training the NN. For testing, the reconstructed radiated photon from $Z \rightarrow \ell\ell\gamma$ ($\ell = e, \mu$) events in data and MC events, and dijet MC events are used.

A photon NN (γ NN4) is built with four input variables as listed in Table I for the EC region. The training is based on direct diphoton and dijet MC events. The same types of events used to test γ NN5 are used to test γ NN4. Considering the similar performance of the input variables of electrons and photons in the EC, γ NN4 is found to work well, and is used, for electron identification in the EC.

Figure 6 shows the NN output distributions for reconstructed EM clusters with $P(\chi_{\text{spatial}}^2) > 0.001$ (electron candidates) and without track match (photon candidates) for $Z \rightarrow ee$ data and MC events, and for dijet background MC events. The distributions show good agreement between data and MC simulation and demonstrate good separation between signal and background.

To validate the photon NNs for jets, dijet data events in the jet-enriched calorimeter isolation region $0.07 < f_{\text{iso}} < 0.15$ are compared to MC simulation. As shown in Fig. 7, good agreement between data and MC is observed.

| Input variables | e NN7 in CC | γ NN5 in CC | γ NN4 in EC |
|----------------------------------------------|---------------|--------------------|--------------------|
| f_{EM1} | ✓ | – | – |
| $N_{\text{cells}}^{\mathcal{R} < 0.2}$ | ✓ | ✓ | ✓ |
| $N_{\text{cells}}^{0.2 < \mathcal{R} < 0.4}$ | ✓ | ✓ | ✓ |
| Σp_T^{trk} | ✓ | ✓ | ✓ |
| $N_{\text{trks}}^{\mathcal{R} < 0.05}$ | ✓ | – | – |
| N_{cps} | ✓ | ✓ | – |
| σ_{CPS}^2 | ✓ | ✓ | – |
| H-matrix χ_{Cal}^2 | – | – | ✓ |

TABLE I: Input variables used in the NNs for electrons and photons in the CC and EC. For electrons in the EC, γ NN4 is used.

C. Boosted Decision Trees for electron identification

To enhance the efficiency and purity in electron identification, a BDT is constructed utilizing variables that are significantly different for signal and background leading

to a strong discrimination power of the BDT output distribution. The following variables are used to construct the BDT:

- EM energy fraction f_{EM} ;
- EM shower isolation f_{iso} ;
- energy fraction in EM1, EM2, EM3, EM4 and FH1;
- σ_ϕ^2 in EM1, EM2, EM3, EM4 and FH1;
- σ_η in EM1, EM2, EM3, EM4 and FH1;
- H-matrix χ_{Cal}^2 ;
- Σp_T^{trk} ;
- cluster-track matching probability $P(\chi_{\text{spatial}}^2)$;
- “hits on road” discriminant D_{hor} in CC;
- ratio E_T/p_T ;
- number of hits from CFT fibers N_{CFT} ;
- number of hits from SMT strips N_{SMT} ;
- ratio $N_{\text{CFT}}/N_{\text{SMT}}$;
- number of hits in the first layer of the SMT;
- number of charged particle tracks with $p_T > 0.5$ GeV originating from the $p\bar{p}$ collision vertex within $\mathcal{R} < 0.05$ of the EM cluster;
- electron likelihood discriminant \mathcal{L} ;
- output distribution of e NN7 in CC;
- output distribution of γ NN4 in EC;
- squared width of the energy deposit in the CPS σ_{CPS}^2 in CC;
- χ^2 for matching the spatial positions between CPS cluster and EM cluster in CC.

For the training of the BDT $Z \rightarrow ee$ and dijet data are used. The BDT is trained separately for the CC and EC and for high ($\mathcal{L}_{\text{inst}} > 1.6 \times 10^{32} \text{ cm}^{-2}\text{s}^{-1}$) and low instantaneous luminosities ($\mathcal{L}_{\text{inst}} < 1.6 \times 10^{32} \text{ cm}^{-2}\text{s}^{-1}$) leading to a different ranking of the utilized input variables. The training of separate BDTs for CC and EC is of advantage since the signal-to-background ratio is different in the two calorimeter regions, and the CC has a better coverage by the tracking devices. Similarly, differences in the signal-to-background ratio and in the resolution of various variables motivate the training of separate BDTs for high and low instantaneous luminosities.

The BDT output distributions are shown combined for all instantaneous luminosities but separately for CC and EC in Fig. 8. They represent the most powerful identification variables among the methods presented here. Typically, the signal efficiency is increased by 4%–8% while

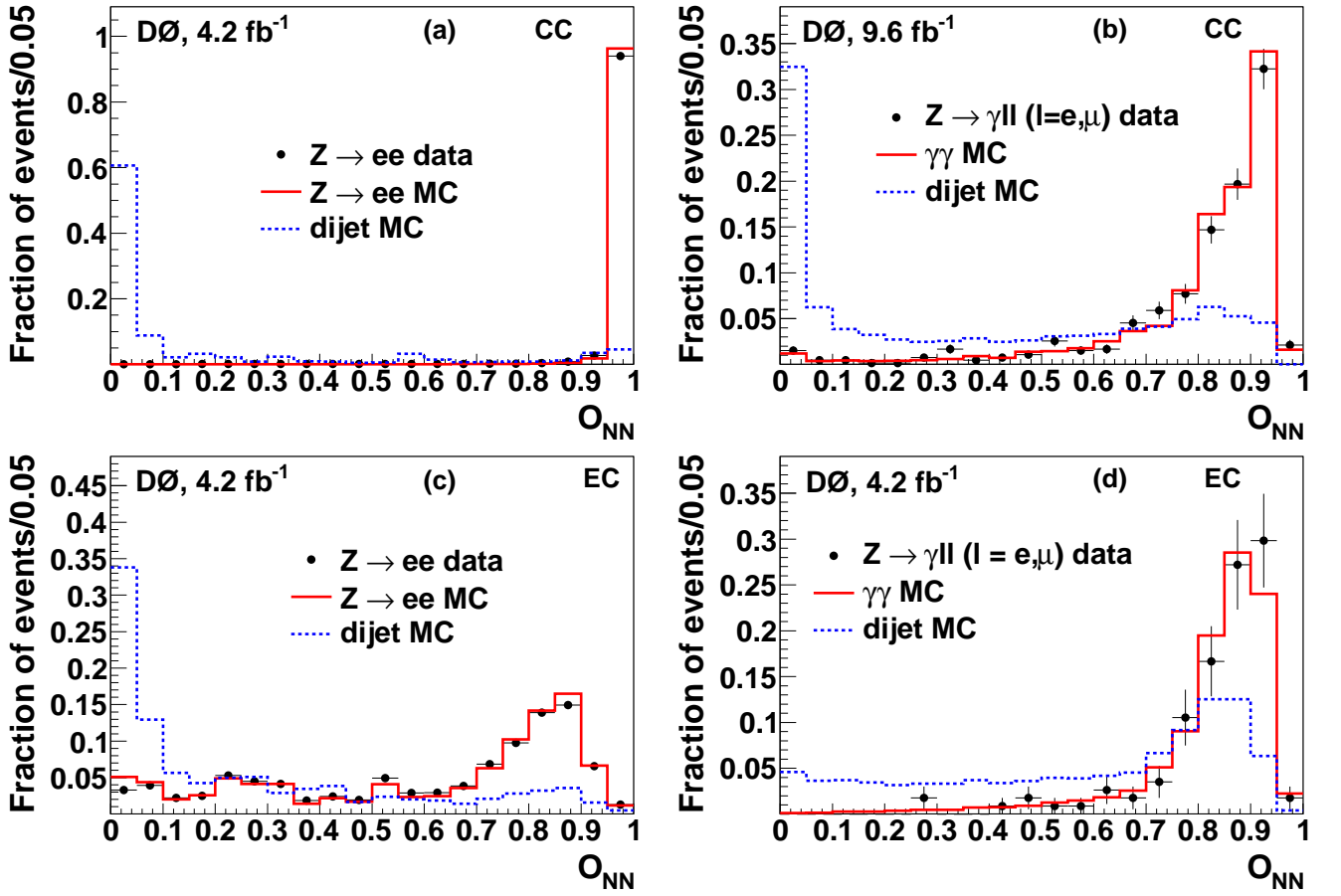


FIG. 6: The output distributions of eNN7 for CC electrons (a), γ NN5 for CC photons (b), γ NN4 for EC electrons (c) and EC photons (d).

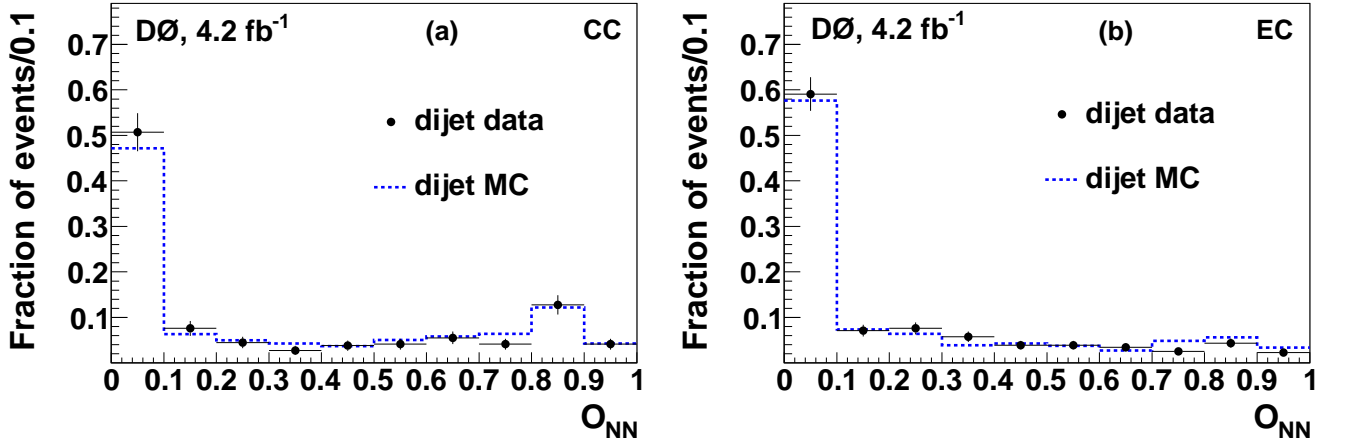


FIG. 7: The output distributions of γ NN5 in CC (a) and γ NN4 in EC (b) for jet-like EM cluster candidates from dijet data and MC events.

maintaining a similar fake rate as other methods. Due to the insufficient description of uninstrumented material in the MC simulation, discrepancy between data and MC exists. This has been studied and taken into account by applying corrections to the simulation.

VI. ENERGY SCALE AND RESOLUTION CALIBRATION

After EM objects are identified as described in Sects. IV and V, the detector response to the energy of

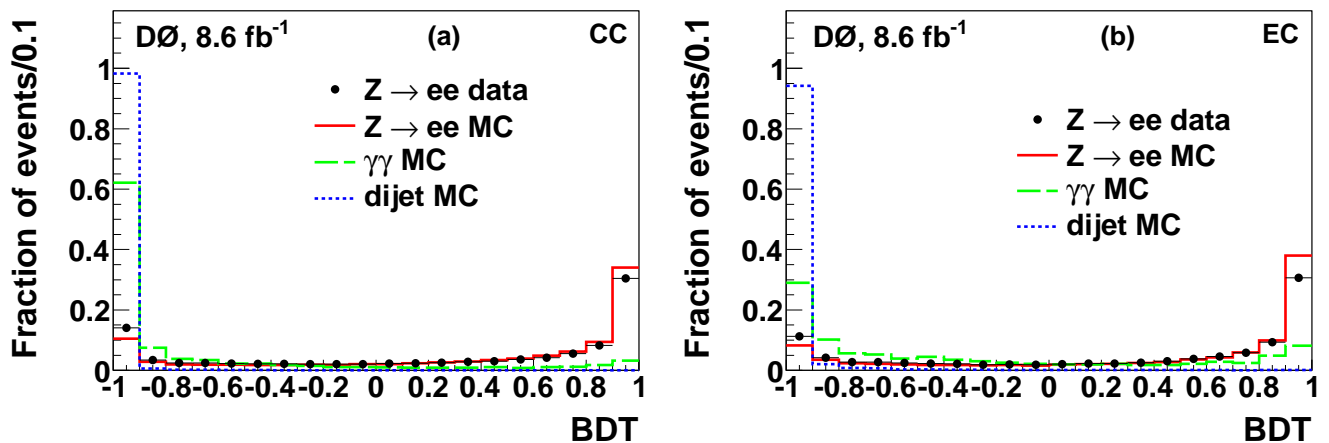


FIG. 8: BDT output distributions of electron candidates in the CC (a) and EC (b) region for $Z \rightarrow ee$ data and MC events, and for dijet and diphoton MC events.

electrons and photons is calibrated. The electron energy scale and resolution are determined from $Z \rightarrow ee$ data events. EM showers induced by electrons and photons have similar distributions in the D0 calorimeter. However, EM clusters deposit energy in the passive material such as the inner detector and solenoid before reaching the calorimeter. On average, electrons lose more energy in this material than photons [16]. To account for this difference, MC simulations tuned to reproduce the response for electrons in data are used to derive the response difference between electrons and photons. In this section, the electron energy scale and resolution, and the energy scale difference between electrons and photons, are described.

A. Energy scale

The amount of material in front of the calorimeter varies between 3.4 and 5 X_0 in the CC and between 1.8 and 4.8 X_0 in the EC [2]. The fraction of energy deposited in each longitudinal layer of the calorimeter depends on the amount of that passive material. The energy loss in passive material is studied taking into account the energy profile dependence on the incident angle [17]. The differences of the energy response between data and the MC simulation are determined using $Z \rightarrow ee$ events and the corrections are applied to the MC simulation.

The energy response is degraded near the module ϕ boundaries for the EM layers of the CC. In addition to a degradation of energy response, the centroid position of the EM cluster is shifted. To study these effects, the following variable is defined:

$$\phi_{\text{mod}} = \text{mod} \left(\frac{16 \cdot \phi_{\text{EM}}}{\pi}, 1 \right), \quad (11)$$

where ϕ_{EM} is the azimuthal angle of the EM cluster.

For track-matched electrons, ϕ_{mod} is determined by extrapolating the associated track through the known magnetic field towards the calorimeter. For photons and non-track-matched electrons, an average correction of the ϕ_{mod} is applied which was determined from track-matched electrons. Regions of $0.1 < \phi_{\text{mod}} < 0.9$ are referred to as “in-fiducial”, the values outside this range are defined as “non-fiducial”. Figure 9 shows the dielectron invariant mass (M_{ee}) distribution for $Z \rightarrow ee$ data events with two CC electrons. The distribution is shown separately for events with 0, 1, and 2 electrons located in fiducial regions. Electrons in or close to module boundaries suffer significant energy losses. To correct for such energy loss, the ϕ_{mod} dependent energy scale corrections are derived for both data and MC simulation using $Z \rightarrow ee$ events. Due to the different amount of material traversed by the electrons before reaching the calorimeter, the events are split into five η regions to derive the correction parameters. In addition, the energy loss near ϕ boundaries is larger for electrons with a poorly measured shower shape corresponding to a large H-matrix χ_{Cal}^2 . The energy scale corrections are therefore derived as a function of ϕ_{mod} and H-matrix χ_{Cal}^2 .

With increasing $\mathcal{L}_{\text{inst}}$ during Run II, the uncalibrated Z boson mass is shifted to lower values in data events. The cause of this effect is discussed in Ref. [2]. The MC simulation, however, predicts an increase in the average EM energy with $\mathcal{L}_{\text{inst}}$ due to extra energy from additional $p\bar{p}$ interactions. In the data, calibration of the calorimeter largely corrects for this energy scale dependence on $\mathcal{L}_{\text{inst}}$. Residual offline corrections are derived by fitting the distribution of E_T/p_T for electrons in $W \rightarrow e\nu$ events, taking advantage of the fact that the p_T scale is independent of $\mathcal{L}_{\text{inst}}$.

Individual cells in the EM calorimeter are known to saturate at energies varying from about 60 to 260 GeV, depending on the cell position. As a result, an EM cluster loses on average about 0.5% (6%) of its nominal energy at 300 (500) GeV. A simple correction truncates the energy

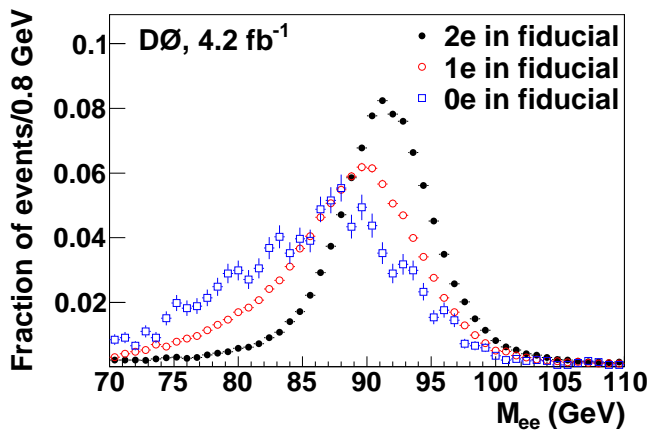


FIG. 9: The M_{ee} distribution in a sample of $Z \rightarrow ee$ data events, where both electrons are in the CC, and separating events with 0, 1 and 2 fiducial electrons. All three distributions are normalized to unit area.

of any cells in the MC that exceed the saturation value for that cell.

Due to the different amount of energy loss between electrons and photons in the passive material, the photon energy is over-corrected by applying the electron energy scale correction. The correction is about 3% at $p_T = 20$ GeV, and it decreases at higher energies. The correction required for forward photons is slightly smaller. The reconstructed photon energy is corrected accordingly to compensate for the over-correction.

The systematic uncertainty for the electron energy scale correction is $\approx 0.5\%$, which is mainly caused by the limited statistics of $Z \rightarrow ee$ data events. For photons, additional 0.5% systematic uncertainty is added in quadrature from electron-to-photon energy scale correction.

B. Energy resolution

The energy resolution of the calorimeter as a function of the electron/photon energy, E , can be written as

$$\frac{\sigma_{EM}}{E} = \sqrt{C_{EM}^2 + \frac{S_{EM}^2}{E} + \frac{N_{EM}^2}{E^2}} \quad (12)$$

with C_{EM} , S_{EM} and N_{EM} as the constant, sampling and noise terms, respectively. The constant term accounts for the non-uniformity of the calorimeter response. Its effect on the fractional resolution is independent of the energy, and therefore it is the dominant effect at high energies. The sampling term is due to the fluctuations related to the physical development of the shower, especially in sampling calorimeters where the energy deposited in the active medium fluctuates event by event because the active layers are interleaved with absorber layers. The noise term comes from the electronic noise of the readout system, radioactivity from the Uranium, and

underlying events. Since the noise contribution is proportional to $1/E$ it is basically negligible for high energy electrons/photons. Due to the large amount of material in front of the calorimeter, S_{EM} is not a constant and is parametrized as a function of electron energy and incident angle [2]. The constant term C_{EM} is derived by a fit to the measured width of the $Z \rightarrow ee$ peak [2]. These terms are measured and applied to the true energy of electron for the fast simulation.

The electron and photon energy resolution predicted by the GEANT-based [11] simulation of the D0 detector is better than observed in data. Furthermore, there are non-Gaussian tails in the resolution distribution that are poorly modeled by the fully simulated MC described in Sect. III, partly because the finite charge collection time of the readout system of the calorimeter is neglected in the simulation. To account for both effects, an ad-hoc smearing is applied to the reconstructed energy of EM clusters following the GEANT simulation according to the following function, which was introduced by the Crystal Ball Collaboration [18]:

$$f(x; \alpha, n, \bar{x}, \sigma) = \begin{cases} \exp(-\frac{(x-\bar{x})^2}{2\sigma^2}), & \text{for } \frac{x-\bar{x}}{\sigma} > -\alpha \\ (\frac{\alpha}{n})^n \exp(-\frac{\alpha}{n}) (\frac{\alpha}{n} - \alpha - \frac{x-\bar{x}}{\sigma})^{-n}, & \text{for } \frac{x-\bar{x}}{\sigma} \leq -\alpha \end{cases} \quad (13)$$

Here, the σ parameter determines the width of the Gaussian core part of the resolution. The α parameter controls the energy below which the power law is used, and the n parameter governs the exponent of the power law. The \bar{x} parameter is the mean of the Gaussian core part of the resolution. Typically, an increase in the width of the non-Gaussian tail needs to be compensated by an increase in the mean. The mean of $f(x)$ is around 0, and the simulated energy is scaled by $1+x$, where x is sampled from the probability distribution function according to Eq. 13.

To determine the parameters of Eq. 13, a fit is performed by varying parameters applied to the MC, and minimizing the χ^2 between the data and fully simulated MC in the M_{ee} distribution. The n parameter is fixed since there is enough freedom in the other three parameters to adequately describe the data. A value of $n = 7$ is found to be appropriate.

The parameters are fitted separately for the following three categories of EM clusters [19]:

- **Category 1: CC in-fiducial**
CC in-fiducial clusters are defined as $|\eta| < 1.1$ and $0.1 < \phi_{mod} < 0.9$. The parameters are fitted using events in which both electrons are CC in-fiducial.
- **Category 2: CC non-fiducial**
CC non-fiducial clusters are defined as $|\eta| < 1.1$ and $\phi_{mod} < 0.1$ or $\phi_{mod} > 0.9$. The parameters are fitted using events containing two CC electrons, where at least one is non-fiducial. Any CC in-fiducial electrons are smeared using their already tuned parameters.

- **Category 3: EC**

EC clusters are defined as having $|\eta| > 1.5$. The parameters are fitted using events containing two EC electrons, or one CC in-fiducial or non-fiducial plus one EC electron. For EC clusters, a simple Gaussian smearing is used where the fit has only two parameters (\bar{x} , σ).

Figure 10 shows a comparison of M_{ee} distributions for $Z \rightarrow ee$ data and MC after applying the energy scale and smearing corrections. Good agreement between data and MC simulation is observed.

VII. EFFICIENCIES OF ELECTRON IDENTIFICATION

Electron trigger, preselection and identification efficiencies are measured in $Z \rightarrow ee$ data and MC events by selecting two high- E_T electron candidates that have an invariant mass close to the Z boson mass peak. To obtain an improved simulation, differences between the efficiencies measured in data and MC simulation are used to derive correction factors to be applied to MC events taking into account kinematic dependences.

A. Tag-and-probe method

To measure the efficiencies, a “tag-and-probe method” is used. In $Z \rightarrow ee$ decays, a $E_T > 30$ GeV electron candidate in CC fiducial is selected as the “tag” with the following requirements:

- $f_{EM} > 0.96$;
- $f_{iso} < 0.07$;
- $\Sigma p_T^{trk} < 2$ GeV;
- associated track $p_T > 15$ GeV;
- $\mathcal{L} > 0.8$;
- $eNN7 > 0.7$.

The “probe” – used to perform the measurement of the identification efficiency – is either an EM cluster or a track. The invariant mass of the tag and probe electrons, M_{tp} , is required to be close to the Z boson mass. If the probe is an EM cluster, M_{tp} is required to be greater than 80 GeV but less than 100 GeV. The energy resolution for high- p_T tracks is worse, and the M_{tp} is required to be greater than 70 GeV but less than 110 GeV when the probe is a track. If the probe passes the tag selection criteria, it will also be used as a tag, resulting in the event being counted twice. To avoid bias, the same tag-and-probe method is used for both $Z \rightarrow ee$ data and MC events.

To remove the residual background from jet production in data events, a template fit is applied to the M_{tp} distributions. The signal shape is obtained from $Z \rightarrow ee$ MC simulation, and the background shape is derived from dijet data. To take into account dependencies on the electron position in the detector, the template fit is performed in various η and ϕ regions. The systematic uncertainty for the tag-and-probe method is dominated by the statistics of $Z \rightarrow ee$ data events. It is $\approx 10\%$ for low probe E_T (< 20 GeV) region, and $\approx 3\%$ for high probe E_T region.

B. Trigger efficiencies

There are two types of single electron triggers [2, 20]. One class of triggers is solely based on calorimeter information and the other class includes tracking information. Calorimeter-based triggers are used for both electrons and photons. To have higher trigger efficiencies for electrons, we combine both types of triggers by taking their logical OR. The tag-and-probe method is used to measure the trigger efficiencies in data. To be consistent with offline electron identification requirements (described in Sect. VII D), the trigger efficiencies are measured with respect to each set of electron identification requirements. To account for dependencies on the EM cluster position in the detector, the trigger efficiencies are parametrized as a function of E_T and η of the electron candidate. Single electrons are triggered with an efficiency $\approx 100\%$ for transverse momenta above 30 GeV in the fiducial regions of the calorimeter up to $|\eta| < 2.5$.

C. Preselection efficiencies

Preselected electrons and photons are EM clusters that satisfy the criteria described in Sect. IV A. The preselection efficiency is given by the fraction of tracks that match an EM cluster passing the preselection requirements for the probe electron candidate. In Fig. 11a the preselection efficiencies are presented for probe tracks in the CC as a function of ϕ_{mod} for data and the MC simulation. The average efficiency is $\approx 98\%$. Data and MC simulation show good agreement, except in non-fiducial regions. Therefore, the ϕ_{mod} -dependent correction factors as shown in Fig. 11a are applied to MC to improve the simulation. Figure 11b shows the preselection efficiencies as a function of η for EC electrons. Efficiency losses are observed in the region $|\eta| > 2.5$ due to partial detector coverage for increasing η . To correct for data versus MC differences in the EC region, η -dependent factors are applied to the simulation. No significant differences between data and MC in other variables are observed for either electrons or photons in the CC and EC regions.

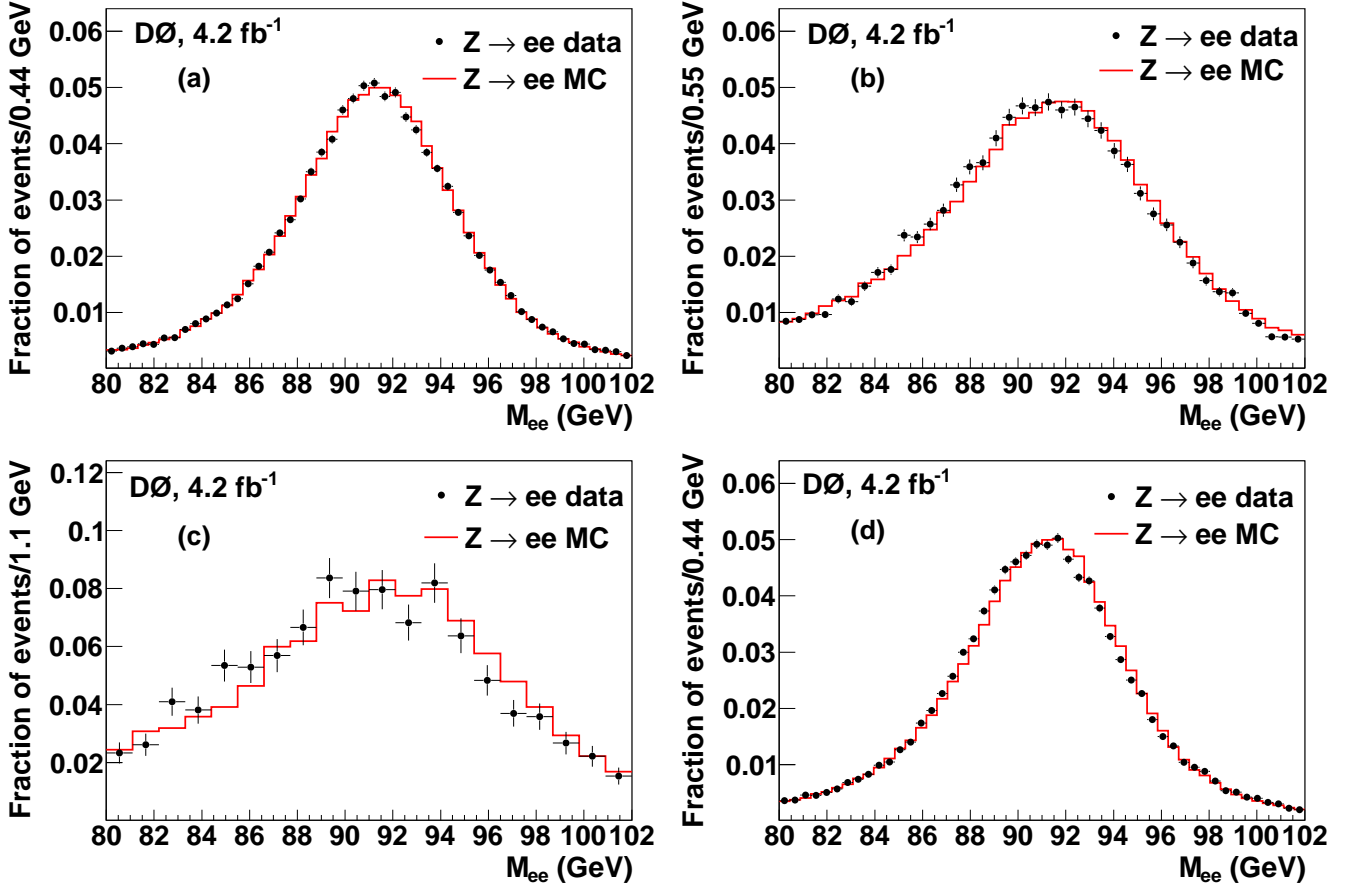


FIG. 10: Dielectron invariant mass (M_{ee}) distributions for $Z \rightarrow ee$ data and MC events, with two electrons in the CC fiducial regions (a), one electron in the CC fiducial region and the other in the CC non-fiducial region (b), two electrons in the CC non-fiducial regions (c), and at least one electron in the EC region (d).

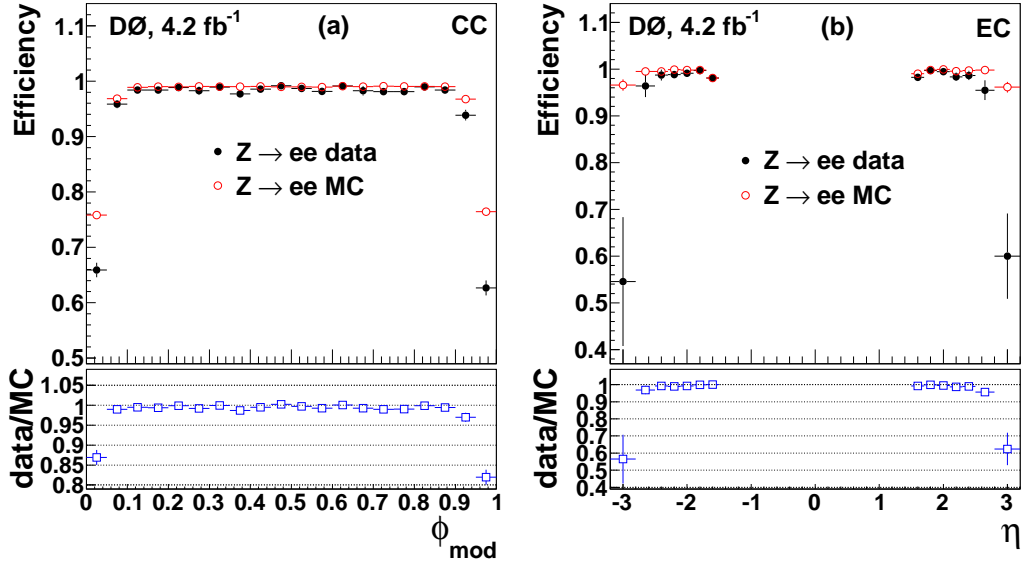


FIG. 11: Preselection efficiencies of probe tracks as a function of ϕ_{mod} and η for electrons in the CC (a) and EC (b). $Z \rightarrow ee$ data is compared to the MC prediction, and the ratio data/MC is presented.

D. Electron identification efficiencies

Many sets of requirements for electron identification are provided for use in physics analyses, each with different electron selection efficiencies and misidentification rates. As examples, the electron identification efficiencies for two sets of requirements are presented here. These sets are called “loose” and “tight”. Table II lists the specific requirements of these two operating points.

The tag-and-probe method described in Sect. VII A is used here with the exception that now the probe electron is required to fulfill the preselection criteria. The identification efficiencies are measured in $\eta - \phi$ phase space. The resulting efficiencies for electrons in data and MC events and the ratio of efficiencies in the data and the MC simulation are shown in Figs. 12 and 13. In CC, the efficiencies in the $\eta \approx 0$ region are lower than in other regions since the light yield of the CFT is lower due to a shorter path length through the scintillating fiber. In EC, the efficiencies decrease in high η region due to the partial coverage of the tracking system. The dependence of the efficiencies on ϕ are mainly caused by the azimuthal variations of the CFT waveguide length not taken into account in simulation.

To account for deficiencies of the simulation, the simulation is corrected by applying η and ϕ dependent correction factors. The dependence on instantaneous luminosity for the electron reconstruction efficiencies is studied and derived following $(\eta - \phi)$ -dependent correction. Relative to the efficiency at low instantaneous luminosity ($\mathcal{L}_{\text{inst}} < 1.5 \times 10^{32} \text{ cm}^{-2}\text{s}^{-1}$) the efficiency decreases with increasing $\mathcal{L}_{\text{inst}}$, declining by $\approx 10\%$ when $\mathcal{L}_{\text{inst}} = 2.5 \times 10^{32} \text{ cm}^{-2}\text{s}^{-1}$. The ratio of those efficiencies in data and MC simulation has no dependence on the instantaneous luminosity.

For transverse momenta of 40 GeV after preselection, loose electrons have a total identification efficiency of 85% (95%) with a fake rate from misidentified jets of 5% (3%) in the CC (EC). Tight electrons at the same transverse momentum have an identification efficiency of 72% (53%) with a misidentification rate of 0.2% (0.1%) in the CC (EC).

VIII. EFFICIENCIES OF PHOTON IDENTIFICATION

A. Photon identification efficiencies

There are two categories of variables for photon identification. Variables based mainly on shower information are used to reject misidentified jets. Tracking-based variables are used to separate electrons from photons. There are two main mechanisms by which photons can appear as electrons. First, if the photon has converted into an electron-positron pair in the inner tracking system, creating a reconstructed track. The probability for conversion is $\approx 6\%$, and we do not reconstruct these converted pho-

tons explicitly. Second, if a track from particles of the underlying event is pointing to the EM cluster. In both cases, the matched track information for a photon will tend to be different from a real electron.

Because a large sample of pure photons is not available in data, $Z \rightarrow ee$ events are used to derive efficiencies for variables based mainly on the calorimeter information. For tracking-based variables, the efficiencies are measured from reconstructed radiated photons in $Z \rightarrow \gamma\ell\ell$ ($\ell = e, \mu$) events in data and MC. In both cases, differences between data and MC event samples are analyzed to correct the efficiency in simulation.

Due to different needs in various physics analyses, various sets of photon identification requirements are developed. We provide here photon identification efficiencies for two different sets of photon identification requirements.

The first set of photon identification requirements considered is used in the search for $H \rightarrow \gamma\gamma$ decays [21, 22]. The signal is dominated by high- p_T CC photons, and the analysis maximizes the photon signal acceptance. Photon candidates in the CC are required to fulfill the preselection requirements as described in Sect. VII C. In addition, it is required that

- $\Sigma p_T^{\text{trk}} < 2 \text{ GeV}$;
- $\sigma_\phi^2 < 18 \text{ cm}^2$;
- Output of $\gamma\text{NN5} > 0.1$.

In addition the following requirements are placed on track-based variables:

- $P(\chi_{\text{spatial}}^2) = -1$;
- $D_{\text{hor}} < 0.9$.

The measured identification efficiencies using the non track-based variables in this selection are presented in Fig. 14 (left column) as a function of E_T , η and ϕ . The differences between data and MC are at the percent level and are constant in the presented distributions. Therefore, a single correction factor is applied to MC photon simulation.

The second set of photon identification requirements presented here is used for measurements of electroweak cross sections, such as the measurement of the $W\gamma$ production cross section [23]. Here, the photons tend to have low E_T and a high background rejection is required. The EC photons used are required to fulfill the preselection criteria of Sect. VII C and to satisfy the following requirements:

- $\Sigma p_T^{\text{trk}} < 1.5 \text{ GeV}$
- $\sigma_\phi^2 < (7.3 \cdot \eta^2 - 35.9 \cdot |\eta| + 45.7) \text{ cm}^2$
- Output of $\gamma\text{NN4} > 0.05$

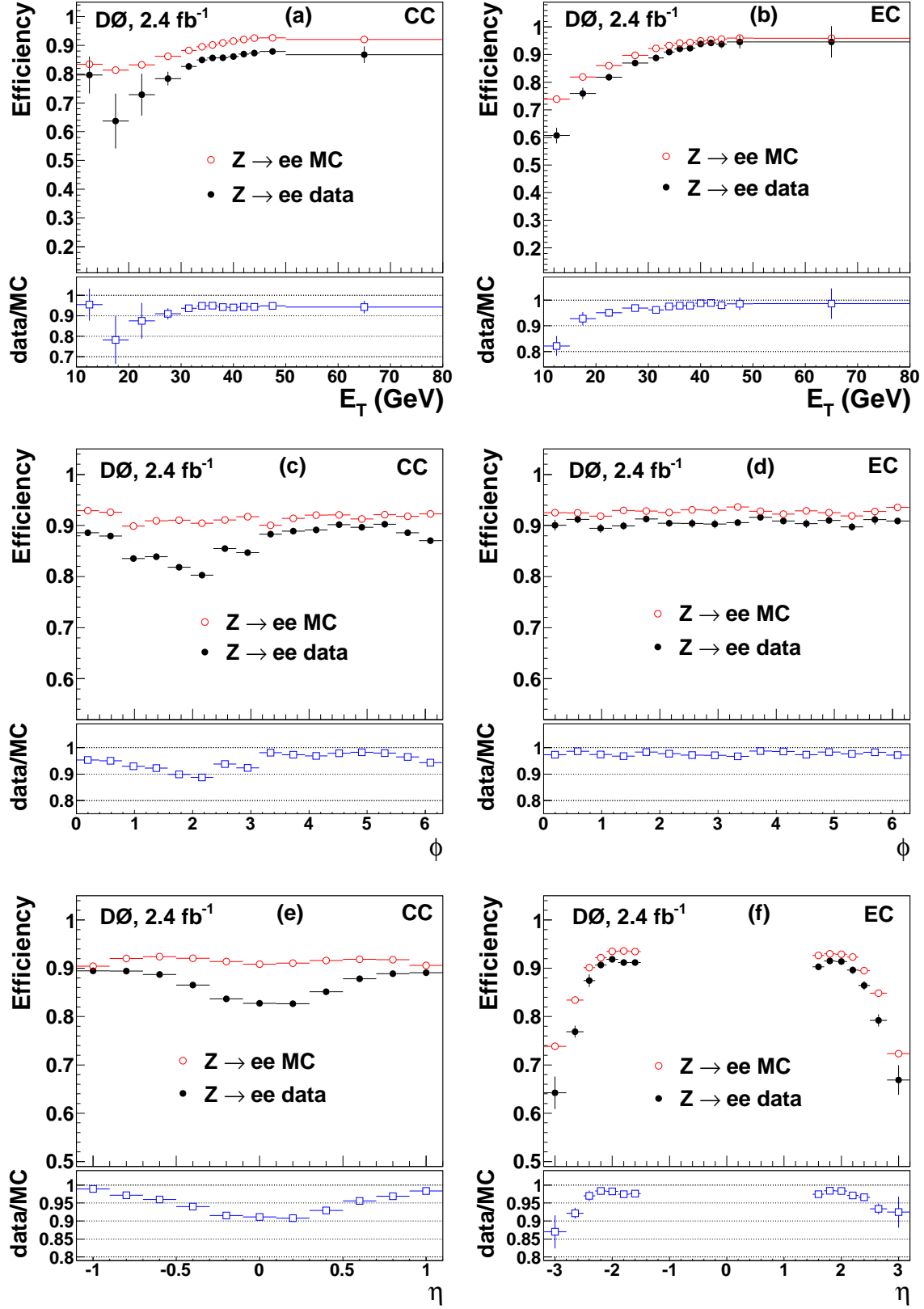


FIG. 12: Electron identification efficiencies as a function of (a,b) E_T , (c,d) ϕ and (e,f) η for loose electron requirements in CC and EC. Efficiencies for data and MC simulated $Z \rightarrow ee$ events are shown, as is the ratio of the data and MC efficiencies.

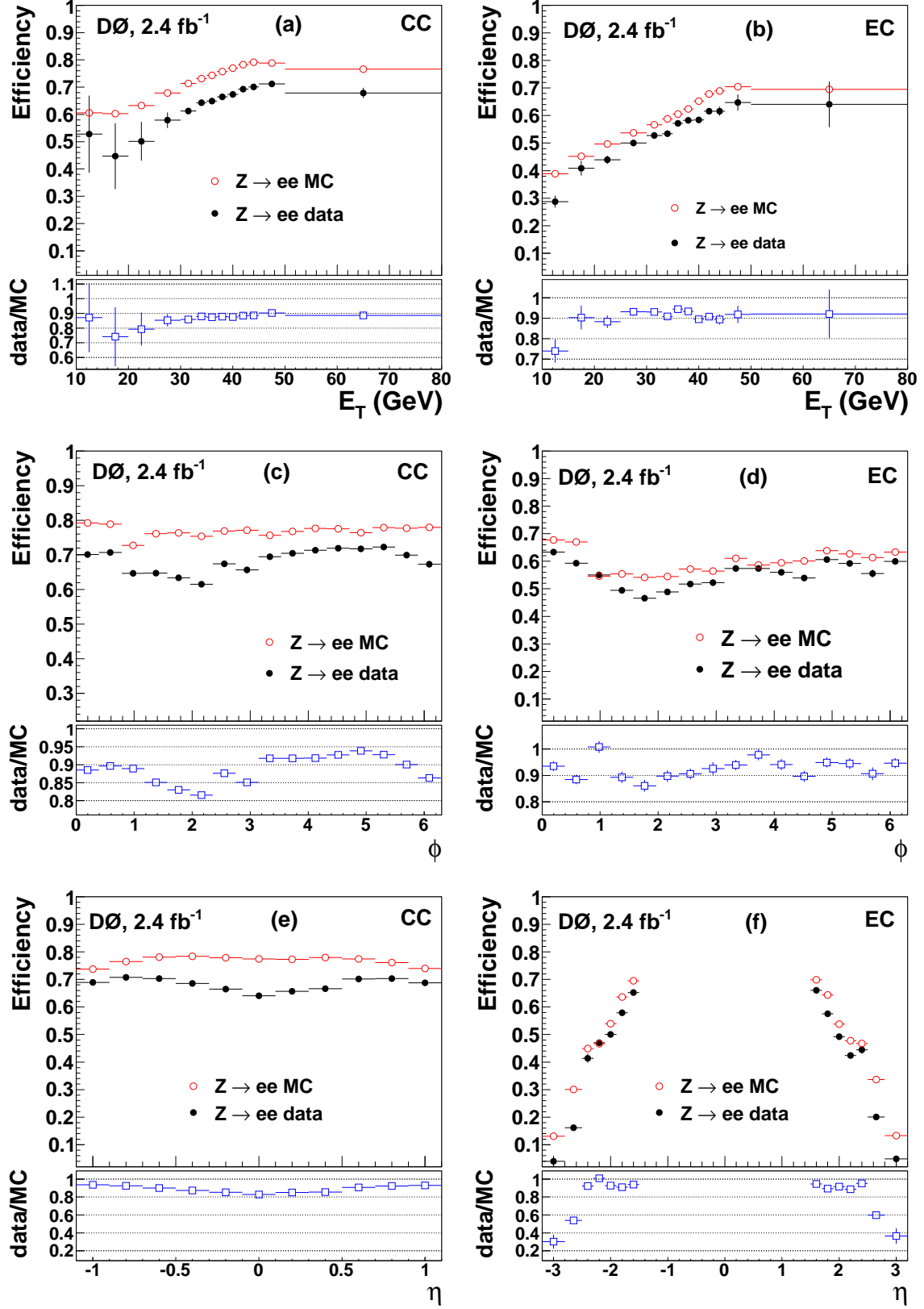


FIG. 13: Electron identification efficiencies as a function of (a,b) E_T , (c,d) ϕ and (e,f) η for tight electron requirements in CC and EC. Displayed are data and MC predictions in $Z \rightarrow ee$ decays and their ratio.

| Variable | loose CC | loose EC | tight CC | tight EC |
|------------------------------------------------------------|-----------|----------|----------|----------|
| $f_{\text{EM}} >$ | 0.9 | 0.9 | 0.9 | 0.9 |
| $f_{\text{iso}} <$ | 0.09 | 0.1 | 0.08 | 0.06 |
| $\Sigma p_T^{\text{trk}} <$ | 4 GeV | (*) | 2.5 GeV | (*) |
| H-matrix $\chi_{\text{Cal}}^2 <$ | – | 40 | 35 | 40 |
| $\sigma_\phi^2 <$ | – | (+) | – | (+) |
| $e\text{NN7(CC)}, \gamma\text{NN4(EC)} >$ | 0.4 | 0.05 | 0.9 | 0.1 |
| $P(\chi_{\text{spatial}}^2) \neq$ or $D_{\text{hor}} >$ | -1 0.6 | – | -1 – | -1 – |
| $\mathcal{L} >$ | – | – | 0.6 | 0.65 |
| $E_T/p_T <$ | – | – | 3 | 6 |

TABLE II: Sets of requirements to identify electrons with loose and tight quality.

(*): $\Sigma p_T^{\text{trk}} < 0.01$ GeV or $\Sigma p_T^{\text{trk}} < (-2.5|\eta| + 7.0)$ GeV

(+): $(6.5 \times (|\eta| - 0.82)^{-1} - 2.8)$ cm² for $|\eta| < 2.6$; $(6.5 \times (|\eta| - 1.35)^{-1} - 2.8)$ cm² for $|\eta| > 2.6$

In addition, a track-based requirement $P(\chi_{\text{spatial}}^2) < 0.001$ is applied.

Figure 14 (right column) shows the identification efficiencies using the non track-based variables in this selection for data and MC. The difference between data and simulation depends on η . To take this into account, the correction to MC simulation is parametrized as a function of η .

For both CC and EC photons, exploring the track-based variables as presented in this section, the efficiencies to identify a photon candidate are measured. The $Z\gamma \rightarrow \gamma\ell\ell$ ($\ell = e, \mu$) data and MC comparison justifies that no further corrections to the photon simulation are required. The photon identification efficiency for these track-based variables is 92% (95%) in CC (EC) for an electron-to-photon misidentification rate of 2% (23%) in CC (EC) in the selections described above. The average photon identification efficiencies for the two sets of requirements described above are 81% and 83% for a rate to misidentify jets as photons of 4% and 10% for CC and EC photons, respectively. These identification efficiencies have a similar dependence on the instantaneous luminosity as the electron identification, and there is no visible dependence on the instantaneous luminosity for the ratio of those efficiencies in data and MC simulation.

B. Vertex pointing

In most physics applications, it is important to know from which $p\bar{p}$ collision vertex the photon originated. Since unconverted photons leave no track, the default reconstruction vertexing algorithm does not provide high probability to find the correct photon origin if there is no high- p_T track in the event. For events without leptons and with energetic photons, the most probable photon production vertex can be reconstructed due to the presence of the underlying event coming from interactions of spectator quarks, and corresponds to the vertex with highest track multiplicity [21, 22, 24]. In such cases, verifying that the true production vertex is found in data is

important, especially in the high-instantaneous luminosity regime with many $p\bar{p}$ collision vertices.

To find the position of the photon origin along the beam line (z -axis) between -60 cm and 60 cm in the CC, the (x, y, z) -coordinates of the EM cluster in the EM1–EM4 layers and the position of the CPS cluster are used. Therefore, 5 points are used with radii from about 73 cm to 99 cm. Using a linear extrapolation to the z -axis, the most probable position of the photon origin vertex is obtained. Typical resolution of the algorithm varies between 3 and 4.5 cm. It becomes larger towards high η mainly due to increasing amount of material in front of the calorimeter (from about 3.4 to $5X_0$). The resolution has been tested in data using $Z(\rightarrow \ell\ell) + \gamma$ events, in which the “true” vertex (z_{true}) is reconstructed using the two lepton (e or μ) tracks and the photon vertex (z_{point}) is obtained using the procedure described above. The distribution of events for $\Delta z = z_{\text{true}} - z_{\text{point}}$ is shown in Fig. 15. The resolution is 2.4 cm for $|\eta| < 0.4$, and 4.3 cm for $0.8 < |\eta| < 1.1$.

The resolution in MC simulation is a factor of 1.4–1.5 better than in data events. To calibrate the pointing resolution, a smearing procedure as a function of photon pseudorapidity is applied. The Δz resolution is almost independent of photon p_T .

IX. CONCLUSIONS

The precise and efficient reconstruction and identification of electrons and photons by the D0 experiment at the Tevatron $p\bar{p}$ collider at Fermilab is essential for a broad spectrum of physics analyses, including high precision SM measurements and searches for new phenomena.

In this paper, the electron and photon reconstruction and identification algorithms have been presented using data collected by the D0 detector in $p\bar{p}$ collisions at a center-of-mass energy of 1.96 TeV. The separation between electron or photon signal and multijet background is considerably improved using multivariate analysis techniques. A likelihood method for electron identification, a

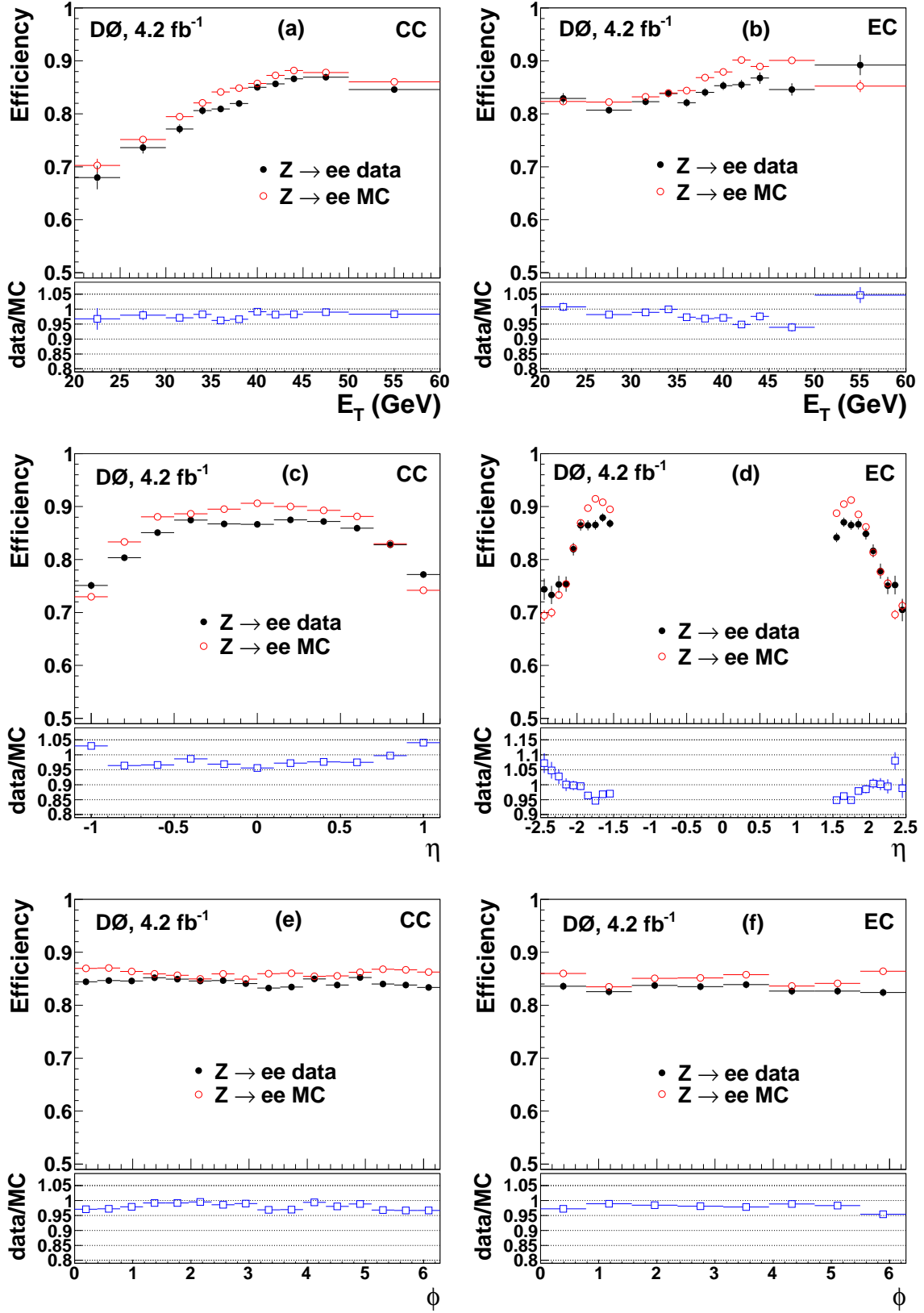


FIG. 14: Photon identification efficiencies for identification variables mainly based on calorimeter information as derived from $Z \rightarrow ee$ decays. Displayed are data and MC predictions and their ratio as a function of E_T (a) (b), η (c) (d) and ϕ (e) (f) for CC and EC photons.

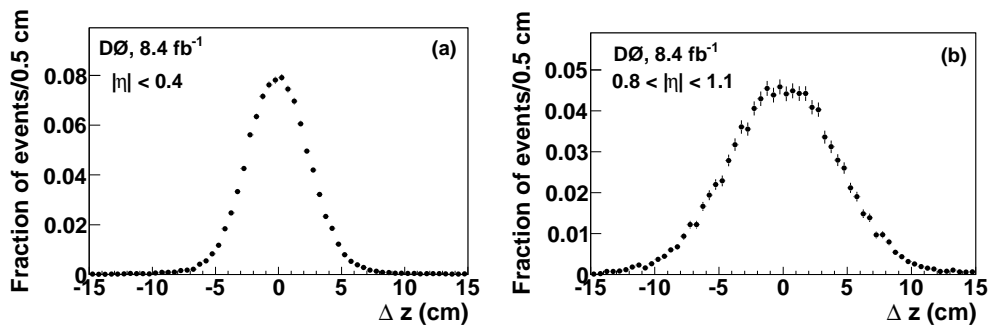


FIG. 15: Vertex pointing resolution in two rapidity bins: $|\eta| < 0.4$ (a), and $0.8 < |\eta| < 1.1$ (b).

neural network method for electrons and photons, and a Boosted Decision Tree for electrons have been developed. An energy calibration dependent on the azimuthal angle of the EM cluster, the shower shape and the pseudorapidity has been performed separately for data and MC, leading to significant improvements in resolution and uniformity and resulting in a good agreement between data and MC.

Single electrons are triggered with an efficiency $\approx 100\%$ for transverse momenta above 30 GeV in the fiducial regions of the calorimeter up to $|\eta| < 2.5$. For transverse momenta of $E_T = 40$ GeV, in general at D0 electrons can be identified with a total identification efficiency of 90% (95%) with the rate at which jets are misidentified as electrons being 5% (3%) in the CC (EC). Photons in the CC and EC regions can typically be identified with efficiencies varying between 69%–84% with the rate at which electrons or jets are misidentified as photons being 2%–10%.

The agreement of electron and photon identification efficiencies between data and MC in fiducial regions of the detector is reasonable, with deviations only at the per-

cent level. Larger correction factors are necessary in non-fiducial regions close to the boundaries of the calorimeter modules. These correction factors have been applied to MC events as a function of kinematic variables resulting in considerable improvements of the simulation.

Acknowledgments

We thank the staffs at Fermilab and collaborating institutions, and acknowledge support from the DOE and NSF (USA); CEA and CNRS/IN2P3 (France); MON, NRC KI and RFBR (Russia); CNPq, FAPERJ, FAPESP and FUNDUNESP (Brazil); DAE and DST (India); Colciencias (Colombia); CONACyT (Mexico); NRF (Korea); FOM (The Netherlands); STFC and the Royal Society (United Kingdom); MSMT and GACR (Czech Republic); BMBF and DFG (Germany); SFI (Ireland); The Swedish Research Council (Sweden); and CAS and CNSF (China).

-
- [1] V. M. Abazov *et al.* (D0 Collaboration), Nucl. Instrum. Methods Phys. Res., Sect. A **565**, 463 (2006).
[2] V. M. Abazov *et al.* (D0 Collaboration), Phys. Rev. D **89**, 012005 (2014).
[3] V. M. Abazov *et al.* (D0 Collaboration), Phys. Rev. D **85**, 052001 (2011).
[4] V. M. Abazov *et al.* (D0 Collaboration), arXiv:1312.6873 [hep-ex].
[5] V. M. Abazov *et al.* (D0 Collaboration), Nucl. Instrum. Methods Phys. Res., Sect. A **737**, 281 (2014).
[6] V. M. Abazov *et al.* (D0 Collaboration), Phys. Lett. B **698**, 6 (2011).
[7] M.L. Mangano *et al.*, J. High Energy Phys. **07**, 001 (2003). Version 2.11 is used.
[8] T. Sjöstrand *et al.*, J. High Energy Phys. **05**, 026 (2006). Version 6.409 with Tune A is used.
[9] V. M. Abazov *et al.* (D0 Collaboration), Phys. Rev. Lett. **100**, 102002 (2008).
[10] J. Pumplin *et al.*, J. High Energy Phys. **07**, 012 (2002);
D. Stump *et al.*, J. High Energy Phys. **10**, 046 (2003).
[11] R. Brun and F. Carminati, CERN Program Library Long Writeup W5013 (1993).
[12] R. Engelmann *et al.*, Nucl. Instrum. Meth. **216**, 45 (1983).
[13] S. Abachi *et al.* (D0 Collaboration), Nucl. Instrum. Meth. Phys. Res., Sect. A **324**, 53 (1993).
[14] L. Breiman *et al.*, *Classification and Regression Trees* (Wadsworth, Stamford, 1984). Version v04-01-00 of TMVA is used.
[15] C. Peterson, T. Rognvaldsson and L. Lonnblad, “JETNET 3.0 A versatile Artificial Neural Network Package”, Lund University Preprint LU-TP 93-29. Version 3.5 is used.
[16] R. Wigmans, “Calorimetry”, Oxford University Press (2000).
[17] R. Lopes, Ph.D. thesis, Stony Brook University, FERMILAB-THESIS-2013-13 (2013).
[18] J. E. Gaiser, Ph.D. thesis, SLAC-R-236 (1980), Appendix D.

- [19] M. Vesterinen, Ph.D. thesis, University of Manchester, FERMILAB-THESIS-2011-35 (2011).
- [20] M. Abolins *et al.* (D0 Collaboration), Nucl. Instrum. Meth. Phys. Res., Sect. A **584**, 75 (2008).
- [21] V. M. Abazov *et al.* (D0 Collaboration), Phys. Rev. Lett. **107**, 151801 (2011).
- [22] V. M. Abazov *et al.* (D0 Collaboration), Phys. Rev. D **88**, 052007 (2013).
- [23] V. M. Abazov *et al.* (D0 Collaboration), Phys. Rev. Lett. **107**, 241803 (2011).
- [24] V. M. Abazov *et al.* (D0 Collaboration), Phys. Lett. B **690**, 108 (2010).